Characterization of Commercial Step-Down Converter Performance in the Low Earth Orbit Radiation Environment

by

Alexa Christine Aguilar

Submitted to the Department of Aeronautics and Astronautics
in partial fulfillment of the requirements for the degree of

Master of Science in Aeronautics and Astronautics

at the

MASSACHUSETTS INSTITUTE OF TECHNOLOGY

June 2019

Signature redacted

Author . . . .
Department of Aeronautics and Astronautics
May 22, 2019

Signature redacted

Certified by . . . .
Kerri Cahoy
Associate Professor of Aeronautics and Astronautics
Thesis Supervisor

Signature redacted

Accepted by . . . .
Sertac Karaman
Associate Professor of Aeronautics and Astronautics
Chair, Graduate Program Committee
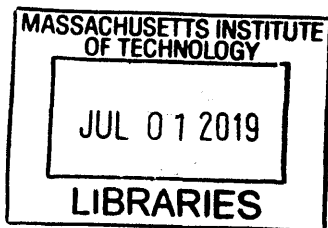
Characterization of Commercial Step-Down Converter Performance in the Low Earth Orbit Radiation Environment

by

Alexa Christine Aguilar

Submitted to the Department of Aeronautics and Astronautics
on May 22, 2019, in partial fulfillment of the
requirements for the degree of
Master of Science in Aeronautics and Astronautics

Abstract

We characterize three commercial step-down DC-DC converters for the Low Earth Orbit (LEO) space radiation environment. Commercial space industry is shifting spacecraft design philosophy toward accepting more risk for shorter lead times, lower costs, and high instrument performance. This shift opens up the Commercial Off The Shelf (COTS) electronics market to space applications. To quantify the risks associated with using COTS parts, components must be tested in flight-like configurations and conditions and their response to environmental stresses characterized. Few data exist in literature on the performance of DC-DC converters in the space radiation environment despite their ubiquity in designs and key role in operation for which the alternative is prohibitively expensive.

This thesis introduces the space radiation environment and resulting effects. We then model the environment for two LEO constellation configurations and determine the maximum expected radiation levels over the mission lifetime. These levels are then used to inform radiation tests.

The DC-DC converters are Total Ionizing Dose (TID) and Single Event Effects (SEE) tested in radiation conditions representative of the LEO space radiation environment. These devices demonstrate radiation tolerance in both tests, with a minimum TID tolerance of 60 krad(Si) and experience no destructive latch-up behavior to about 90 MeV-cm^2-mg^{-1}. A first order reliability analysis shows these parts introduce little additive risk to spacecraft design.

Thesis Supervisor: Kerri Cahoy
Title: Associate Professor of Aeronautics and Astronautics

Acknowledgments

I would first like to thank my advisor Dr. Kerri Cahoy for her guidance and unfailing support during my time at MIT. Her drive and technical prowess are unparalleled and I would not be where I am in my academic and professional career without her.

I would also like to thank Dr. Randall Milanowski for his technical guidance and expertise on radiation. I truly appreciate all the instruction he has offered in using OMERE, designing tests, and interpreting results. Additional thanks to Steve McClure for his knowledge of radiation effects on electronics. Both of their support of this project was instrumental in its success and timeliness.

I would also like to acknowledge Dr. Slaven Moro and Raichelle Aniceto for giving me the opportunity to work on this project. I sincerely appreciate the chance to work in the radiation effects field.

Finally, I would like to thank my parents, Buster and Francie Aguilar, for their unwavering support and encouragement during my time in MIT's Department of Aeronautics and Astronautics.

Contents

List of Figures

12

List of Tables

Chapter 1

Introduction

Predictions by Morgan Stanley estimate the global satellite industry could generate $1.1 billion in revenue by 2040, half of which is attributed to growth of broadband internet [43]. This growth is being driven by exponentially-increasing data demands in applications such as mobile internet, autonomous vehicles, and Internet of Things (IoT) [43]. Satellite communication systems offer an attractive solution to meeting these demands because of their ability to service large areas of low population density with little to no existing infrastructure as well as augment current terrestrial networks.

The barrier to space has historically been the prohibitive costs associated with developing, manufacturing, launching, and operating satellites and user terminals. Recent advances in rocket technology, such as SpaceXs Falcon 9, have reduced launch costs by a factor of 2 [43]. Commercial satellite developers and manufacturers, such as OneWeb, are developing methods to streamline manufacturing and further reduce cost-to-orbit [50]. Despite this progress, a significant hurdle remains for satellite communication systems traditionally operating in the Radio Frequency (RF) regime; the Federal Communication Commission (FCC) requires authorization to transmit in the RF band prior to launch. Securing authorization is an expensive and time-intensive process, often costing companies upwards of $500,000 per application [19] and years of wait-time with no guarantee of approval [25].

Free Space Optical Communication (FSOC), otherwise known as laser communications, operates in the Near Ultraviolet (NUV) to Near Infrared (NIR) regime and

can achieve data rates orders of magnitudes greater than RF for similar Size Weight and Power (SWaP) [40]. Optical bands offer increased gain (narrower beamwidth), increased bandwidth, and higher power efficiency over RF. From a system perspective, these advantages lead to reduced Size, Weight, and Power (SWaP) for equal or greater performance than RF systems.

The space radiation environment presents key operational and design challenges for spacecraft, and careful consideration must be made in selecting both electrical and optical components for laser communication systems. Electronics and materials onboard spacecraft are susceptible to radiation effects, which can lead to system unavailability, functional interrupts, or mission failure. To reduce these risks, mitigation strategies such as shielding and designing with radiation-hardened (rad-hard) electronics are used, however, the costs associated with using rad-hard parts are significant and performance may be limited [34],[51].

To reduce overall system costs, Commercial-Off-The-Shelf (COTS) components can be used in exchange for increased risk. This approach is becoming increasingly popular, particularly for LEO systems where the radiation can be less severe, and companies are releasing intermediate-grade components to service a growing market [37]. In making this trade, the first step is understanding and quantifying the effects of radiation on a subsystem and the implications for system operations. Radiation Hardness Assurance (RHA) ensures selected components and materials of a system perform to specification after exposure to the radiation environment. RHA teams or radiation engineers translate mission parameters into environment definitions, quantify effects on selected parts, develop mitigation strategies at the board, subsystem, or system level, and make recommendations for alternative components if required.

This thesis describes the analysis, testing, and results from characterizing three commercial DC to DC (DC-DC) step-down converters in the Low Earth Orbit (LEO) radiation environment. First, the near-Earth radiation environment is modeled to derive test levels. Next, Total Ionizing Dose (TID) testing and Single Event Effects (SEE) testing is performed to evaluate the response of three devices with applications to space-based laser communication systems. Results show radiation tolerance

up to 100 krad(Si) with unbiased room temperature annealing, and no destructive latch-up behavior across all parts. These results are significant, as uninterrupted and well-characterized performance of power regulators are required for any space-based systems, and few space-rated, commercial-grade DC-DC converters are currently available.

1.1 Motivation for Optical Communications

FCC licensing costs can compete with or exceed launch costs, especially for small satellites [58]. The National Telecommunications and Information Administration (NTIA) of the United States Department of Commerce considers spectrum above 300 GHz to be unallocated and does not currently require authorization for operations [45]. Paired with higher data rates for a given SWaP, laser communication is attractive alternative to RF communication.

Laser communication in commercial satellites is not as pervasive as RF due to key challenges. While narrow beamwidth increases system gain, it requires higher precision pointing control which can be costly on satellites [24]. Solutions to this challenge include widening the transmit beam, supplementing coarse pointing with fine pointing systems, and increasing the effective area of the receiver; however, these solutions either significantly increase system complexity or reduce performance such that optical is comparable to RF systems. Additionally, higher frequencies are subject to more frequent outages introduced by weather and cloud coverage, which is an issue for communication system downlink unavailability [24].

The NASA Space Communications and Navigation (SCaN) program has identified optical communications as a critical technology enabling up to 40x higher data rates with 50% less mass and 25% less power than their RF counterparts [40]. In 2013, The NASA Lunar Laser Communication Demonstration (LLCD) demonstrated a 622 Mbps downlink from the Moon to Earth [10]. Since then, NASA SCaN has developed a family of missions ranging from LEO to deep space dedicated to laser communication demonstrations scheduled out to 2027 [40].

19

1.1.1 Existing Optical Communication Systems

Space-based laser communication systems have successfully demonstrated secure, high data rate capabilities for the last two decades. In 1994, the National Institute of Information and Communications Technology (NICT) partnered with the Japanese Space Agency (JAXA) and demonstrated a 1 Mbps bi-directional link at a range of 37,800 km with the Laser Communication Experiment (LCE) onboard the ETS-VI. LCE mass was 22.4 kg with an average optical output power of 13.8 mW [3].

In 2001, the European Space Agency (ESA) demonstrated the first inter-satellite link at 50 Mbps between geostationary satellite Advanced Relay and Technology Mission Satellite (ARTEMIS) and LEO Satellite Pour IObservation de la Terre (SPOT4) [21]. The link range was published as 40,000 km, and the optical payload, Semiconductor Intersatellite Link EXperiment (SILEX), had a mass of 100 kg [21]. During that same time, the US launched GeoLITE containing an optical payload designed by MIT Lincoln Laboratory. GeoLITE was declared a successful mission but data rates and other system details are not available [41], [42].

JAXA later launched a laser communications payload, Laser Utilizing Communication Equipment (LUCE), on the Optical Inter-orbit Communications Engineering Test Satellites (OICETS) mission. LUCE and SILEX demonstrated the first bi-directional optical communications link in 2005. From LEO to GEO, the data rate was 50 Mbps, and from GEO to LEO, the data rate was 2 Mbps, both at a range of about 40,000 km. LUCE mass was 140 kg with an average optical output power of 200 mW [33].

The German Aerospace Center (DLR) developed Laser Communication Terminal (LCT) flown on the US satellite Near Infrared Experiment (NFIRE) and on a German satellite Synthetic Aperture Radar for Earth Observations (TerraSAR-X) [56]. In 2008, the two payloads successfully demonstrated LEO to LEO crosslinks at 5.625 Gbps at a range of 5000 km [1]. LCT mass was 32 kg and peak optical output power of 700 mW [20].

MIT Lincoln Laboratory designed and developed LLCD, which was launched on-

board the NASA Lunar Atmosphere and Dust Environment Explorer (LADEE) mission. In 2013, LLCD demonstrated an optical downlink to Earth from Lunar orbit (400,000 km) at speeds of 622 Mbps. LLCD mass was 30 kg with an average optical output power of 500 mW [11].

NASA JPL developed the Optical PAyload for Laser Communications (OPALS) system that demonstrated a 50 Mbps downlink from the International Space Station (ISS) in 2014. OPALS mass was 50 kg and average optical output power was about 830 mW [47].

In 2018, NASA and the Aerospace Corporation demonstrated an optical downlink of 100 Mbps from a CubeSat mission AeroCube 7-B and 7-C [54]. AeroCube mass is 2.31 kg and optical output power of 4 W [55].

Table 1.1: Demonstrated Optical Communication Systems

Optical Terminal Name	Payload Mass [kg]	Demo Year	Data Rate [Mbps]	Power Trans- mitted [mW]	Beam Width [μrad]	Link Dis- tance [km]	Link Type
LCE [3], [17]	22.4	1994	1	13.8	30	37,800	GEO to Ground
SILEX [21]	100	2001	50	37	6	38,000	GEO to Ground
LUCE [33]	140	2005	50	100	5.5	38,000	GEO to LEO
LCT [20], [64]	32	2008	5625	700	7.1	5,000	GEO to LEO
LLCD [10]	32	2013	622	500	15	400,000	Lunar Orbit to Ground
OPALS [47]	50	2014	50	$\geq$830	1650	700	LEO to Ground
Aerocube 7B/C [54],[55]	2.31	2018	100	4000	2700	450	LEO to Ground

1.2 Motivation for Commercial Off the Shelf Components

Electronics and materials used in laser communication systems are susceptible to radiation effects, leading to system unavailability, functional interrupts, or mission failure. Until the 1990's, reducing these risks translated to using rad-hard parts whenever possible. This led to the development of highly reliable military- and (aero)space-grade components and testing standards that are widely used today, such as Qualified Manufacturers List (QML) parts and military standard 883 (MIL-STD-883) outlining TID test procedures. Although the probability of failure is greatly reduced by designing with rad-hard parts, Bill of Material (BOM) costs are significantly higher and performance lower than COTS alternatives. A tradespace between risk, cost, and performance has opened, and high reliability COTS components and COTS-based systems are emerging particularly for use in LEO [37].

Moore's Law states that transistor density per device versus relative manufacturing costs doubles every year and predicts a gap between commercial and space microelectronics. Commercial microelectronics in 2019 commonly use 7 nm technology, though the International Technology Roadmap for semiconductors predicts pervasive 5 nm technology by 2020 [28]. Radiation-hardened electronics are highly customized and produced in much smaller quantities than commercial counterparts. "Cutting-edge" space-grade devices use 150 nm technology in 2019 [26]. This performance gap is a key COTS motivator as science and mission objectives have become increasingly complex.

To illustrate the performance gap, we compare a rad-hard system to a COTS system. The Mars Science Laboratory (MSL or Curiosity Rover) launched in 2011 required an unprecedented level of autonomy to traverse the Martian terrain efficiently for its 23-month mission life [31]. The on-board processor is a BAE RAD750 CPU with a maximum clock speed of 200 MHz [5]. For comparison, the first iPhone, which was in development around the same time for a similar lifetime, used an ARM 11 CPU with a maximum clock speed of 620 MHz [4]. Using processing speed as a proxy
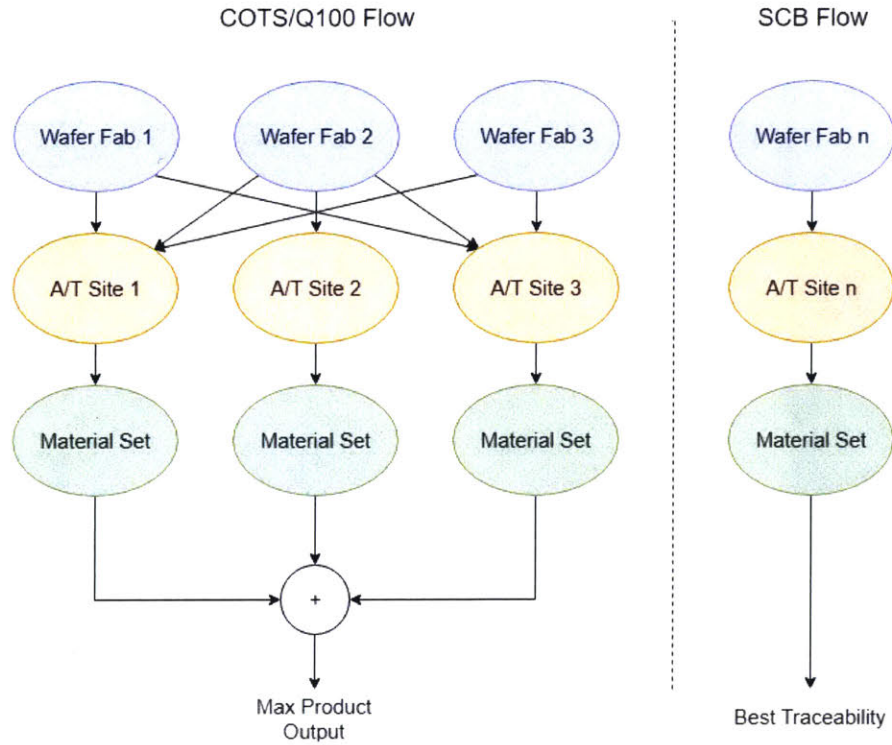
Figure 1-1: Each wafer fabrication facility, assembly and test (A/T) facility, and material set facility change operations and process to optimize for maximum yield locally. Singe Controlled Baseline (SCB) reduces manufacturing variability [7].

for performance, the COTS system (iPhone) has over twice the computing power as the rad-hard system (MSL).

As a result of different levels of risk tolerance, radiation requirements, and performance requirements, microelectronics manufacturers have begun to offer intermediate-grade components designed for higher thermal loads and increased reliability than COTS alone [6]. QML components traditionally use specialized materials, undergo extensive testing to demonstrate radiation-hard characteristics, operate over a wide, military-defined temperature range, use hermetically-sealed ceramic packaging, and come from a single, controlled baseline (SCB) lot, which is crucial for reducing manufacturing variability across devices [7]. Figure 1-1 illustrates production flows for COTS, automotive-grade (Q100), and QML components.

Intermediate-grade components come in plastic packaging from SCB lots. Occasionally, the SCB lots come from QML facilities, ensuring minimal product variation for a fraction of the QML cost [7]. Figure 1-2 shows an example grade spectrum

23

Increasing Component Quality, Reliability, and Cost →

	COTS / COTS+		Enhanced Intermediate Grades			Space Grade	
	Commercial	AEC-Q100	EP	QMLQ	Space EP	QML-V	QMLV-RHA
Packaging	PLASTIC	PLASTIC	PLASTIC	CERAMIC	PLASTIC	CERAMIC	CERAMIC
Single Controlled Baseline	NO	NO	YES	YES	YES	YES	YES
Bond wires	Au or Cu	Au or Cu	Au	Al	Au	Al	Al
Pure Sn Used	YES	YES	NO	NO	NO	NO	NO
Burn-in Performed	NO	NO	NO	NO	NO	YES	YES
Radiation Tested	NO	NO	NO	NO	YES	YES	YES
Radiation Assured	NO	NO	NO	NO	YES	NO	YES
Temperature Range	-40 to 85°C	-40 to 125°C (only grade 1)	-55 to 125°C (majority)	-55 to 125°C	-55 to 125°C (majority)	-55 to 125°C	-55 to 125°C
100% 3 Temp Test	NO	NO	NO	YES	25, 125°C	YES	YES
Extra Qual/Process Monitors	NO	YES	YES	YES	YES	YES	YES
Life Test per lot	NO	NO	NO	NO	NO	YES	YES

Figure 1-2: Component Grade Spectrum from Texas Instruments [6]. Commercial, Automotive (Q100), Enhanced Performance (EP), and Qualified Manufacturers List (QML) components span the range of available parts.

matrix. An example of SCB importance is found in work by Lacoe on two lots of the same 0.35 um Hewlett Package transistors [14]. The first lot showed excellent performance to TID levels of 300 krad(Si) with no leakage current; however, the second lot, dated three months later than the first, showed significant leakage current at TID levels of 70 krad(Si) [14]. Widely-varying radiation performance across the same device is a barrier to the test like you fly philosophy, and screened devices could behave differently than flight hardware.

Selecting a component grade is a complex trade that depends on radiation requirements, mission lifetime, and total acceptable risk [37]. If COTS are selected for a mission, an up-screening process is required to ensure the device meets performance specifications in the radiation environment [37]. COTS up-screening is performed by environmentally stressing and electrically testing parts beyond their guaranteed operating ranges to characterize performance under these conditions. Radiation Hardened by Design (RHBD) methodology supports COTS-based systems by incorporating fail-safe modes tailored to known device faults found during up-screening which decreases risk [36]. This approach is becoming increasingly popular as designs move away from
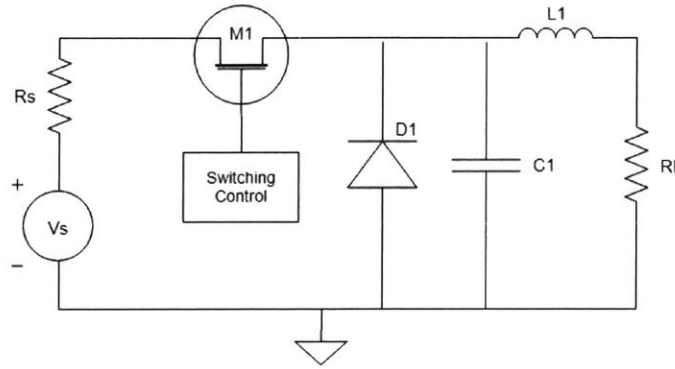
Figure 1-3: Typical buck converter topology.

device-level radiation hardening to system-level radiation hardening [37].

1.2.1 Motivation for Commercial DC-DC Converters

Satellite systems require Electrical Power Systems (EPS) capable of supplying power for the duration of the mission with tolerance to transients, and bus and load faults. Computational loads on science payloads are projected to increase with the utilization of laser communication. Managing the total required power requires high efficiency power electronics, such as the DC-DC converters used in power distribution.

DC-DC converters are a type of power electronic often used in power subsystems to regulate or smooth battery power to a specific voltage and current before connecting to the power bus. Output levels define the type of DC-DC converter; devices that maintain higher outputs relative to inputs are step-up or boost converters; devices with lower outputs are step-down or buck converters; devices with both functionalities are buck-boost converters. Figure 1-3 shows a buck typical buck converter topology where V_S is the input voltage to be reduced, R_S is the source resistance, $M1$ is the switch modulated by the switching control, $D1$ is the diode that allows continuous current flow when the switch is open, $C1$ and $L1$ elements act as energy storage or filtering elements, and R_L is the load.

Hybrid DC-DC converters, which have better efficiency than traditional DC-DC converters, are more susceptible to radiation effects, particularly transient effects [35]. Hybrid DC-DC converters achieve higher efficiencies by integrating switching control

on the same chip as the converter [13]. Design of a fault-tolerant EPS requires low susceptibility to radiation effects. Although not much information is available from manufacturers on price and lead time without specific inquiry, Table 1.2 highlights a publicly available example by comparing a rad-hard DC-DC converter and a commercial DC-DC converter.

Table 1.2: Comparison of 28V Input Hybrid DC-DC Converters

Manufacturer	PN	Efficiency	Cost per Unit
Infineon (prev. International Rectifier)	LS PD-97812A	81%	$ 10,400 [52] [27]
Texas Instruments	TPS54334	85%	$2.42 [60]

It is evident using rad-hard components to design an EPS may be infeasible for programs under time or budget constraints. Following the new-space philosophy and accepting increased risk for higher performance and lower lead times, it is desirable to shift to designs incorporating commercial DC-DC converters.

Few commercial DC-DC converters have been tested within the last few years, which is relevant because devices are highly sensitive to process variations that are subject to change every few years. Those DC-DC converters that were tested and reported experienced destructive events or non-destructive latch-up [1]. To build cost effective and efficient EPS's to support next generation satellite communication systems, it is imperative to test commercial DC-DC converters and understand failure modes in these devices. If the response is non-destructive, mitigation techniques can be developed such that using these devices for space applications is feasible. This thesis seeks to address this gap by performing TID and SEE testing on 3 DC-DC converters.

1.3 Overview of this work

In this thesis, three commercial step-down (buck) DC-DC converters are analyzed and tested for use in LEO. The maximum output current of these devices are 4 A, 8

A, and 12 A, and will be referred to by this rating. These devices are automotive-grade System-on-Chip (SoC) devices with an integrated power regulation chip and multi-mode functionality. These components have applications to space systems requiring high efficiency EPS and offer a high-reliability, radiation-tolerant, commercial alternative to rad-hard DC-DC converters.

Chapter 2 describes the Earth radiation environment and subsequent radiation effects to provide context on the RHA problem. Two LEO constellations are selected and analyzed to illustrate the impact of mission parameters to radiation requirements and how this influences reliability design. Chapter 3 describes the testing approach and high-level device analysis. The requirements derived in Chapter 2 are used to inform testing levels for TID and SEE testing. Chapter 4 illustrates the experiment setup and presents the results from TID and SEE testing. These findings are significant as they show TID tolerance to 100 krad(Si) with unbiased, room-temperature annealing and no destructive latch-up behavior. Non-destructive behavior is observed, and mitigation strategies are proposed. Upset rates for each device are calculated and reliability analysis is performed for the worst-case upset rate. Chapter 5 presents the conclusion and future work. While these devices exhibit radiation tolerant behavior, uncertainties in both TID and SEE testing can be further reduced to minimize risk in using these parts in space applications.

Chapter 2

The Earth Radiation Environment

In this chapter, we introduce the LEO radiation environment and total dose and single event effects on analog electronics. Through modeling and simulation of the radiation environment, requirements are developed to form a basis for radiation test levels.

2.1 Low Earth Orbit Radiation Environment

There are three sources of radiation in LEO: the Sun, which produces solar energetic particles (SEP); the Van Allen belts, where protons and electrons are trapped within Earth's magnetic field lines; and galactic cosmic rays (GCRs), which are high energy protons or heavy ions originating outside the solar system.

2.1.1 Solar Radiation

Solar activity fluctuates in 11-year half-cycles (22-year full-cycles due to solar magnetic pole reversal) with peaks having a higher number of solar wind and Coronal Mass Ejection (CMEs) events. SEPs primarily consist of high energy protons, electrons, and heavy ions, and are transported to Earth via solar winds and CMEs. Within SEPs, proton energies range from 500 keV to 100s of MeV, and heavy ion energies from 1 MeV to 1 GeV, with particle fluences reaching 10^{10} particles/cm^2 during a

solar maximum. The Earth's magnetosphere shields against electrons, but because protons and heavy ions have higher energies (or masses), they are not as easily impeded by the magnetosphere. As a result, SEPs in LEO are primarily protons, and thus events associated with SEP are called Solar Proton Events (SPEs) [22].

2.1.2 Trapped Particles

The Van Allen Belts (radiation belts) are toroidal regions of electrons and protons trapped by Earth's magnetic field. The first region, or inner belt, extends from a few 100s of km to ~6,000 km altitude and is dominated by high energy (~10s of MeV) protons, but also contains high energy (1-10 MeV) electrons. The second region, or outer belt, extends out to 60,000 km altitude and is predominately high energy electrons. Figures 2-1 and 2-2 illustrate the structure and integral flux of electrons and protons.
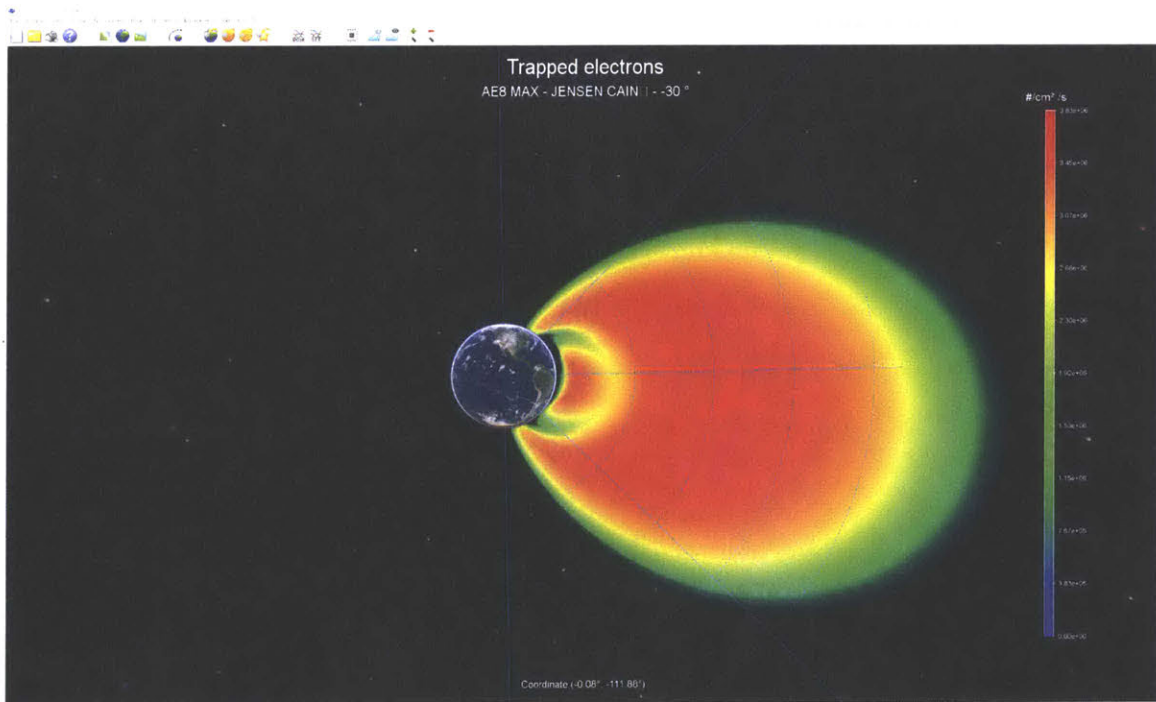
Figure 2-1: Integral flux of Trapped Electrons generated using OMERE 5.2.2 using the AE8 model for trapped electrons with the Jensen Cain Model, according to ECSS-10 Standards.

Trapped particles are postulated to come from terrestrial (Cosmic Ray Albedo
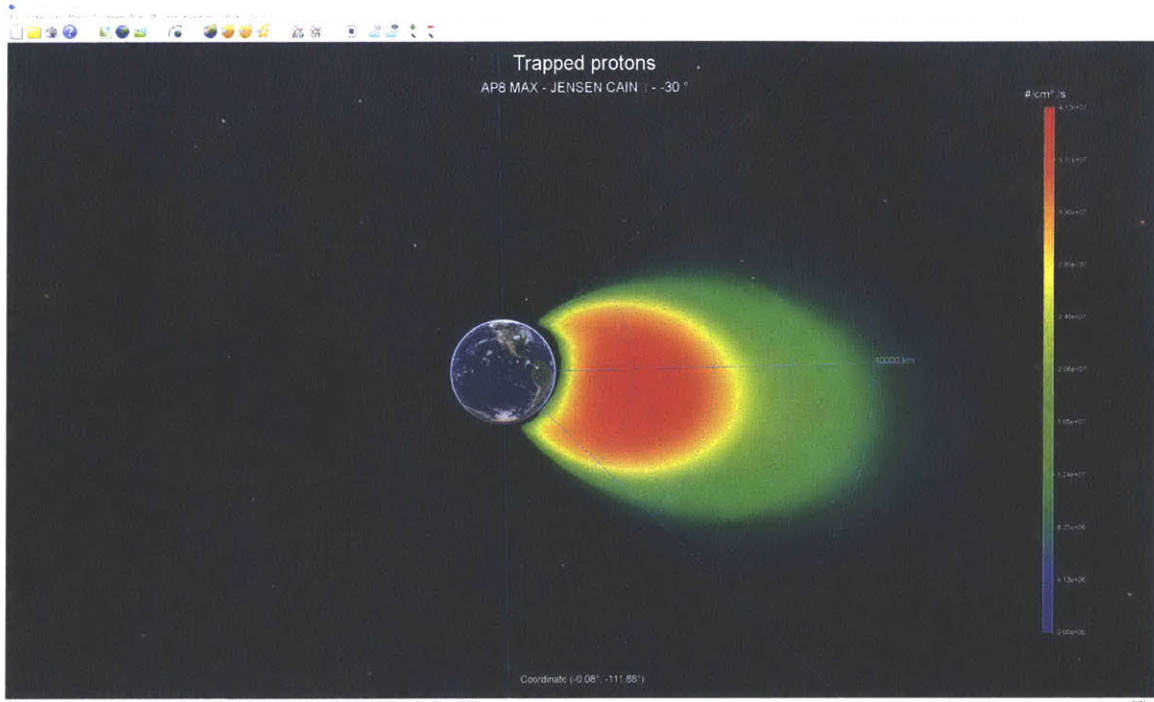
Figure 2-2: Integral flux of Trapped Protons generated using OMERE 5.2.2 using the AP8 model for trapped electrons with the Jensen Cain Model, according to ECSS-10 Standards.

Neutron Decay) and interplanetary sources (solar wind) and are subject to large temporal variations. The inner belt structure is relatively stable as it is governed by Earth's magnetic field, but variations correlated with solar cycle and Ionosphere dynamics are seen. The outer belt is more dynamic as it is governed by Earth's fluctuating geomagnetic tail. Earth's magnetic field axis and rotational axis are offset by an ~11-degree northward tilt and 500 km separation. A weaker magnetic field region results above the south Atlantic near southeast Brazil allowing high energy protons to dip lower into Earth's atmosphere. This region is known as the South Atlantic Anomaly (SAA) and is slowly drifting westward with a period of ~1200 years [22]. Figure 2-3 shows increased particle flux levels in the SAA region.

2.1.3 Galactic Cosmic Rays

Galactic Cosmic Rays (GCRs) are the third source of radiation in the near-Earth radiation environment. Originating outside of the solar system, GCRs consist primarily
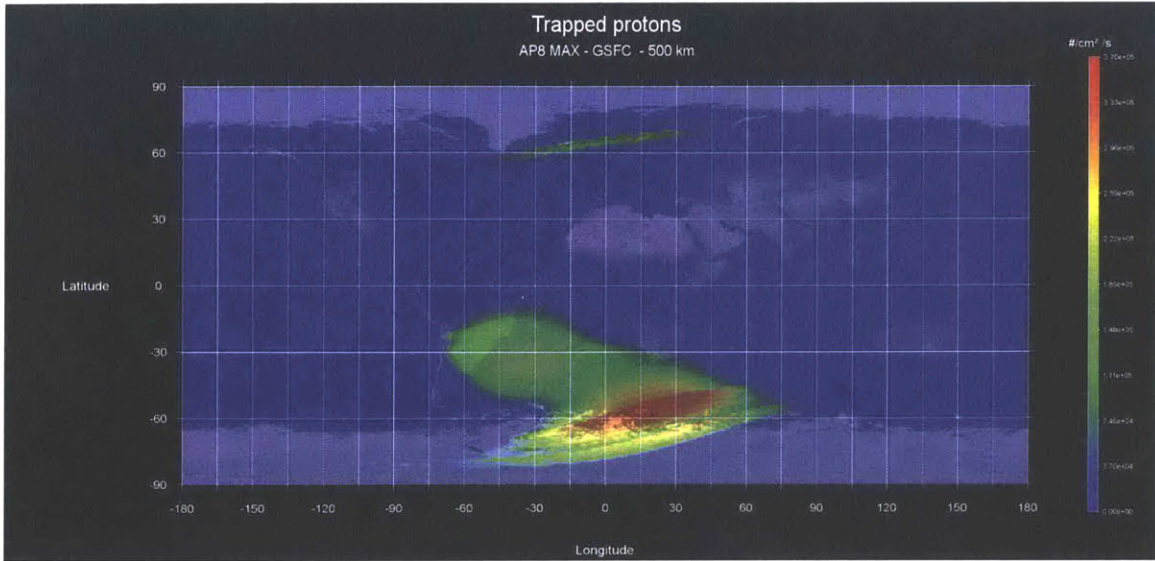
Figure 2-3: Increased proton flux known as the South Atlantic Anomaly at lower latitudes due to the offset in Earth's magnetic field axis and rotation axis.

of high energy protons, heavy ions, and electrons ranging from ~1 MeV to 10GeV in energy. These particles interact with Earth's atmosphere and cause Extensive Air Showers (EAS) creating cascades of secondary particles resulting from nuclear interactions. These showers of secondary particles consist of high energy neutrons, electrons, and protons and disintegration particles such as pions and muons. GCR activity is inversely proportional to solar activity. During solar maximums, GCR intensity is at a minimum and vice versa. This relationship is attributed changes in the solar wind magnetic field. More turbulent winds present during solar cycle maximums scatter GCRs more effectively and inhibit their propagation to the inner solar system. As the solar winds recede and relax during solar cycle minimums, GCRs more easily penetrate the near-Earth environment.

The Lorentz force from Earth's magnetic field acts as a shield against GCRs (and solar winds). Particles with trajectories parallel to magnetic field lines experience no Lorentz force. The approximate dipole structure of the Earth's magnetic field results in higher levels of atmospheric interaction and particle showers at higher latitudes.
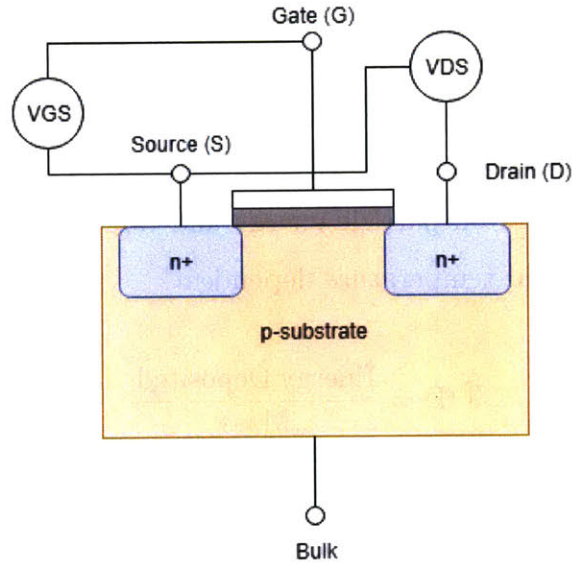
Figure 2-4: Cross-section and corresponding device representation of a Metal Oxide Semiconductor Field Effect Transistor (MOSFET). The device activitates and allows current to flow between the Drain (D) and Source (S) when the Gate (G) voltage exceeds the voltage between D and S.

2.2   Radiation Effects on Electronics in LEO

Radiation present in the near-Earth environment can adversely affect electronics. Cumulative effects change device operating parameters, degrade performance, and induce leakage currents, while instantaneous or transient events can have destructive or non-destructive effects. A Metal Oxide Semiconductor (MOS) transistor, or MOS-FET, will be used as a reference device to illustrate these effects. MOSFETs are the building blocks of modern integrated circuits. While device-level responses may differ for individual MOSFETs in the presence of radiation, using a simple example develops intuition and understanding of the underlying physics.

The basic application of a MOSFET is a voltage-controlled switch and is show in 2-4. By applying a voltage to the gate exceeding the potential between the drain and source, the MOSFET turns on, and current flows between the drain and source nodes. Within the device, voltage applied to the gate creates a conduction channel between the drain and source enabling current flow. These devices are sensitive to both ionizing and non-ionizing radiation.

33

2.2.1 Total Ionizing Dose

Total ionizing dose (TID) is a cumulative effect caused by incident electrons and protons creating trapped charges within a device. The amount of total charge accumulation or dose depends on particle energy and target material, and the device response to dose is bias and temperature dependent.

$$\text{TID} = \frac{\text{Energy Deposited}}{\text{Mass}} \tag{2.1}$$

The underlying physical mechanism of radiation-induced charge trapping happens on picosecond scales. It takes a finite amount of energy to generate electron-hole pairs in a semiconductor. For the purposes of this thesis, its assumed the oxide is SiO_2, which has a pair creation energy, E_p, of 17 ± 1 eV [49]. Incident ionizing radiation in the oxide layer creates electron-hole pairs where the total number of pairs can be determined knowing the incident particle energy, E_p of the material, and the charge pair volume density per rad $g_0 = 8.1E{+}12 \; \frac{\text{pairs}}{\text{cm}^3-\text{rad}}$.

The initial number of charge pairs is a function of the amount of energy imparted to the material by radiation. This value is known as the Linear Energy Transfer (LET) of a particle which is the change in total energy, dE, over the path the particle takes, dx, normalized by the material density ρ. In particle physics, this is also known as the material stopping power. LET is discussed further in Section 2.2.3. TID can also be expressed in terms of LET.

$$\text{LET} = \frac{1}{\rho}\left(\frac{dE}{dx}\right)_{Ionizing} \tag{2.2}$$

By multiplying LET by the time-integrated integral flux, or fluence ϕ, TID can be calculated.

$$\text{TID} = \phi\text{LET} \tag{2.3}$$

In the first few picoseconds following generation, a fraction of the electrons are carried out of the oxide; the remaining electrons recombine with some of the holes to form stable pairs, but several holes remain unpaired. The final number of holes

34

escaping recombination is a function of the magnitude of the electric field, acting to separate holes and electrons, and the initial number of charge pairs generated by incident radiation. The larger the electric field, the higher the number of holes in oxide layers. Therefore, electronics TID testing involves irradiating both biased and unbiased parts, where biased samples are representative of worst-case charge trapping.

In the case of a Negative-channel MOS (NMOS) transistor, a commonly used technology know for its sensitivity to radiation, radiation-induced charge trapping occurs in the gate oxide layer resulting in gate voltage shifts *i.e.*, over time, less voltage is required to create the conduction channel. If the amount of trapped charge is large enough, devices cannot be turned off. Figure 2-5 illustrates MOSFET pre- and post-irradiation operation.
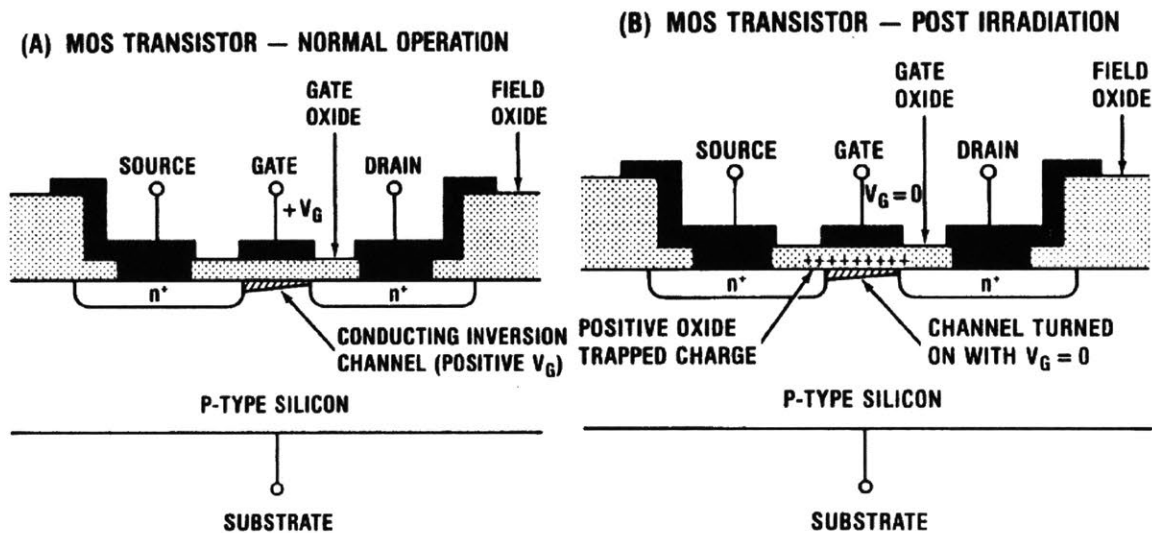
Figure 2-5: MOSFET Operation under nominal conditions (a) and post-irradiation (b). Charge accumulates in the gate oxide over time and reduces the amount of voltage required to turn the device on. Eventually, if the cumulative dose is high enough, a permanent conduction channel will form, and the device cannot be turned off even if 0 V is applied at the gate [49].

The remaining holes create a bulk charge on the gate oxide, shifting the threshold voltage required to operate the device to a lower level. Other technologies susceptible to TID are other MOS transistors (Complementary MOS, Positive-channel MOS), FETs, integrated circuits (ICs), and bipolar junction transistors (BJTs). TID effects in FETs manifest as increased leakage current between the source and drain. Effects

in BJTs result in current gain degradation [49]. Devices utilizing these technologies can exhibit varying sensitivities to TID effects due to variations in process flow (e.g., foundry, time of manufacturing). Serendipitously, as device processes shrink, and gate oxide thicknesses and other susceptible device regions shrink, TID tolerance increases as less charge is trapped within critical regions [49].

Both analog and digital components are susceptible to TID as both use sensitive technologies. In the scope of DC-DC converters, TID is expected to mostly influence the switch preceding the inductor in the main circuit and the control circuit monitoring the output ($M1$ and Switching Controls in Figure 1-3).

2.2.2 Displacement Damage

Displacement damage (DD) is the dominant effect for compound semiconductors without oxides to trap charge (e.g., optoelectronics). DD is strictly concerned with non-ionizing radiation effects and can be expressed in terms analogous to TID. The equivalent of LET for DD is known as non-ionizing energy loss (NIEL) which describes the amount of energy imparted to a material causing nuclear displacement.

$$\text{NIEL} = \frac{1}{\rho} \left(\frac{dE}{dx} \right)_{Non-Ionizing} \tag{2.4}$$

Like TID, the total number of ions through a square centimeter for a given period, or fluence ϕ, multiplied by NIEL gives the total non-ionizing dose contributing to DD.

$$\text{TNID} = \phi\text{NIEL} \tag{2.5}$$

DD occurs when a crystal lattice nucleus (such as Si) is dislodged by an incident particle. The displaced atom settles in an interstitial location, and the previously occupied lattice position contains a vacancy. The interstitial atom and vacancy form a Frenkel pair, which is the simplest form of non-ionizing defects [49]. Different materials have different energy thresholds for displacement damage. Table 2.1 lists some common materials susceptible to displacement damage and corresponding DD

36

energy threshold.

Table 2.1: Displacement damage energy thresholds for common materials susceptible to TNID [49]. Optoelectronics such as photodetectors (PD) will often use these materials.

Material	E_{DD} (eV)
Diamond	35 ± 5
Si	27.5
Ge	21
GaAs	7-11

Displacement damage results in defects to the semiconductor bandgap, which can have significant electrical impacts. The first effect is the generation of an electron hole pair from a "center" energy threshold in the bandgap introduced by DD. This process is also viewed as a hole emission followed by electron emission from the center and dominates in regions where free carrier concentrations are less than thermal equilibrium values (*i.e.*, in depletion regions). Increased leakage current is attributed to the introduction of a DD center.

The second effect results in an increased recombination lifetime. The average time a carrier spends in a band before recombining is defined as the recombination lifetime. The defect creates an energy threshold within the bandgap that attracts both electrons and holes, which results in carrier recombination and reduces the time each carrier spends in a band. Gain reduction in bipolar technology is attributed to this mechanism.

The last effect is trap assisted tunneling, wherein carriers tunnel from either the valence or conduction band to the other due to DD-induced defects, creating free charge carriers on both ends. In MOS transistors, the result is higher current levels.

Optoelectrical devices are sensitive to displacement damage as they lack oxides to trap charge induced by radiation [49]. Other sensitive devices include bipolar technologies such as BJTs and MOS transistors. In the scope of DC-DC converters, DD is not expected to be the dominant radiation-induced degradation and will likely be masked by TID defects.

2.2.3 Single Event Effects

Single Event Effects (SEE) are unwanted or erroneous responses from an electronic device caused by a charged particle passing through the active region of the device. Protons, neutrons, and heavy ions can evoke SEE through direct or indirect ionization mechanisms.

In direct ionization, the charged particle interacts directly with electrons in target material, freeing them from their bound states and leaving a wake known as a charge track. Heavy ion interaction in material typically results in direct ionization as they carry the highest amounts of charge. In indirect ionization, the charged particle interacts with the nuclei of the target material (as in displacement damage), and the recoiling nuclei interact with electrons.

Heavy ions are responsible for mostly direction ionization SEE as they carry the highest amount of charge; additionally, they leave the densest charge tracks of all SEE particles. SEE caused by protons are predominantly the result of indirect ionization, however, smaller process nodes more susceptible to SEE show sensitivity to proton direct ionization. Converse to the improved TID performance, device shrinkage increases SEE vulnerability because of reduce charge capacity, and devices operating terrestrially have reported functional disruptions due to SEE [8]. Neutrons solely contribute to indirect ionization as they carry no net charge and do not electrically interact with electrons.

As charged particles interact with a target material, they lose kinetic energy. The linear rate of energy loss is the known as the Linear Energy Transfer (LET) which was mentioned in Section 2.2.1. LET is a function of target material density and the path of the particle through the material (Equation 2.2). The units of LET are energy per unit mass per unit area, or MeV-cm^2-mg^{-1}.

It is useful for testing purposes to see LET vs. range curves for a target material (*i.e.* how much energy is lost as a function of distance traveled by a particle). The LET vs. range curve reveals the maximum energy lost in a material as well as maximum range of ion and is formally known as a Bragg curve. Figure 2-6 illustrates
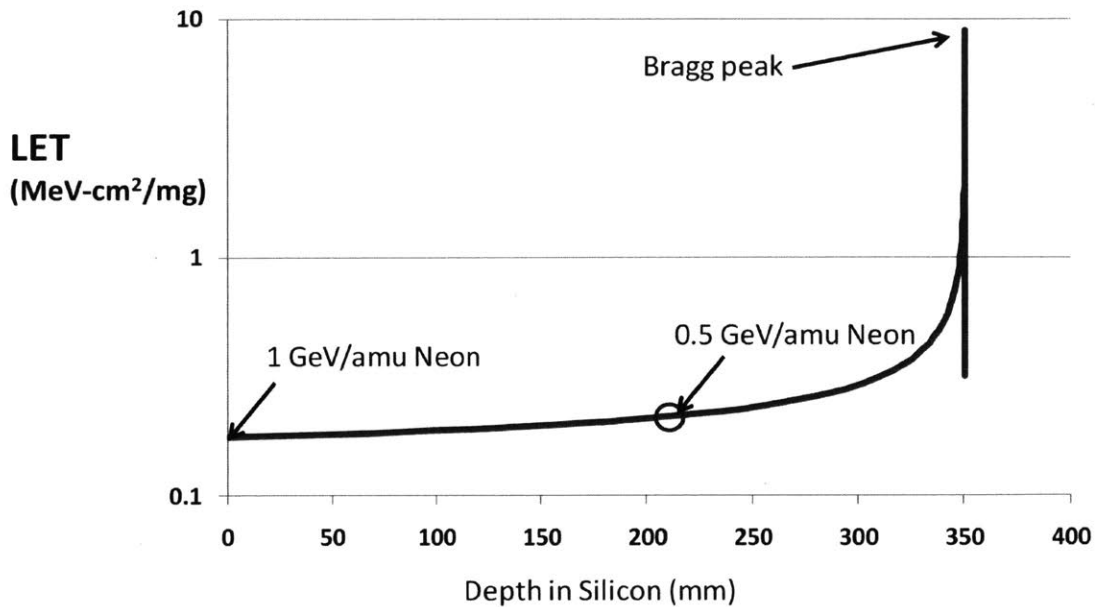
Figure 2-6: Bragg Curve for Neon in Silicon. Initial Energy for Neon is 1 GeV. Bragg peak occurs at 350 mm [8].

an example of a Bragg curve with a Neon particle incident on a Silicon target material. Note the maximum range is roughly 350 mm and the maximum LET is ~9.5 MeV-cm^2-mg^{-1}. When the charged particle approaches the region where its kinetic energy is comparable to the imparted energy, LET increases dramatically with range. Initially, the energy lost is low because the velocity of the particle relative to the velocity transferred to the electrons is low. When these values approach equality, a masking effect occurs where the electrons mask the apparent charge of the particle, and the LET decreases dramatically near the end of the ion range [8].

There is a range of behaviors a device may exhibit after a particle hit. Analog and digital devices share some responses, but others are specific to domain. Table 2.2 lists events and device responses broken into two categories: destructive and non-destructive. A non-destructive event implies a device will return to nominal operation after a power cycle or at the end of the upset while a destructive event permanently alters the functionality of the device.

In the scope of DC-DC converters, relevant effects include SET and SEL events.

39

Table 2.2: Single Event Effects Relevant to Hybrid DC-DC Converters

	Event	Description
Destructive	Single Event Latch-up (SEL)	Abnormal high-current state in a device due to turn-on of parasitic BJT by an energetic particle resulting in loss of device functionality.
	Single Event Gate Rupture (SEGR)	Breakdown and creation of subsequent conducting path through gate oxide.
	Single Event Burnout (SEB)	Localized high current state resulting in catastrophic device failure or permanent degradation that is characterized by a significant increase in leakage current exceeding manufacturer's maximum specification.
Non-Destructive	Single Event Transient (SET)	Momentary voltage excursion at a node in an integrated circuit.
	Single Event Functional Interrupt (SEFI)	Interruption resulting from single ion strike causing component to reset, hang, or enter different operating condition or test mode.
	Single Event Upset (SEU)	Change of a bi-stable node state from one to zero, or vice-versa.
	Multiple Bit Upset (MBU)	Upset of multiple cells where two or more of the error bits occur in the same logical word.

For applications requiring stable input voltages, transients could disrupt functionality and lead to gaps in operation. Latch-up events require power resets, also creating potential gaps in operation. In worst-case scenarios, latch-up is destructive and could lead to mission failure.

The SEL mechanism is attributed to the presence of parasitic BJTs within CMOS. Figure 2-7 illustrates a simple CMOS transistor with two parasitic BJTs imposed on the cross section for visualization. A CMOS device consists of several PNP and NPN junctions, each creating a BJT. In the illustrated example, a lateral and vertical BJT are formed. When a charged particle strikes a CMOS device, track of dense charge is left it its wake. Carriers are swept away and the current spike results in a regenerative
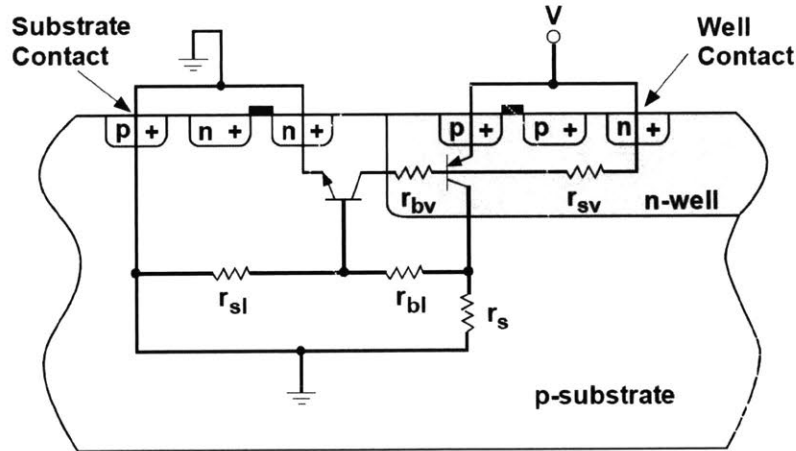
Figure 2-7: Cross section of CMOS transistor showing parasitic BJTs. Each NPN and PNP junction creates a parasitic BJT within a CMOS device. When current flows through these regions, a regenerative gain state is activated, creating a run-away current state. Resistances are from the bulk and substrate materials [8].

gain state of the BJTs. The newly flowing current is met with resistance from the bulk and substrate materials denoted by r_{sl} and r_{bl} in the lateral BJT and r_{sv} and r_{bv} in the vertical BJT. The results of this high current state may be destructive as the device fails from thermal effects or cracked dielectrics or non-destructive, which is difficult to prove, as latent damage is often revealed in post-testing analysis [38].

In summary, particles in the LEO radiation environment can cause radiation effects in spacecraft. Particles may have multiple effects depending the on the target device, and particle fluence varies with solar cycle and Earth's magnetic field. Figure 2-8 summarizes the types of energetic particles from key sources and subsequent effects.

2.2.4   Upset Rate Calculations

To quantify the SEE performance of a device, data is required for a known environment configuration. The event cross section, σ, is defined as the expected value of the event rate per flux, or total events per particle fluence. Note the units of σ are cm^2, but σ is a probability density function and does not correspond to a physical area. The cross section of a device depends on type of event (*e.g.*, SET or SEL), incident
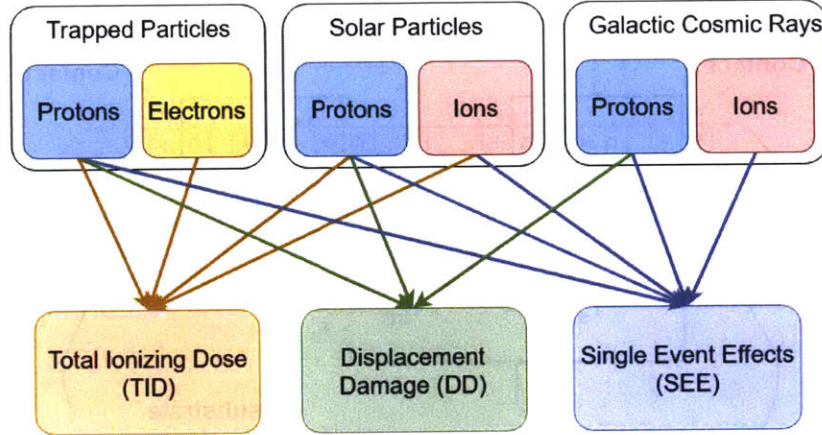
Figure 2-8: Summary of energetic particles and radiation effect contributions.

particle energy and subsequent LET, the particle angle of incidence, and circuit test parameters and configuration (*e.g.*, circuit bias, temperature, clock speed, etc.).

$$\sigma = \frac{\text{Total Number of SEE}}{\text{Particle Fluence}} \quad [\text{cm}^2] \qquad (2.6)$$

Once the cross section is calculated for each event type of interest, it can be plotted against corresponding LET values, creating what is known as the cross-section curve. Figure 2-9 shows a notional cross-section curve. Key parameters of the cross-section curve are the saturation cross section, σ_{sat}, at which the cross-section saturates (1E-2 in the example curve) and LET_{onset}, which is the lowest LET at which an no events are observed (~ 2 MeV-cm^2-mg^{-1} in the example curve). The onset LET is also known as the threshold LET.

The cross-section curve can be used to determine the upset rate or event rate for any given orbit. This is critical in developing mitigation strategies and performing failure analyses as it describes the rate at which a device will experience SEE. Depending on the type of SEE, the failure mode may require a power cycle, so the upset rate may also be used to inform the frequency of power resets. In general, the upset rate is given by Eq. 2.7.

$$\text{UpsetRate} = \text{Flux(orbit)} * \sigma \quad \left[\frac{\text{events}}{\text{sec}}\right] \qquad (2.7)$$

42
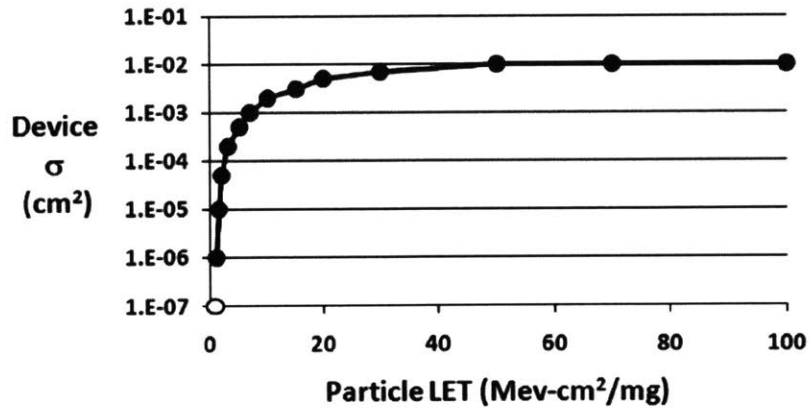
Figure 2-9: Notional Cross Section Curve for a device with target material of Silicon. Note the cross section curve is sensitive to ion incident angle [8].

The generalized solution uses σ integrated over the LET spectrum of the orbit, which requires a function fit to the data. Early computational models used a step function, however this led to overestimates of event rates due to the additional area introduced by the step-function fit. The solution to better estimates was to apply a cumulative Weibull function to the data.

$$\sigma(\text{LET}) = \sigma_{sat} \left(1 - \exp\left(\left(\frac{LET_0 - LET}{W} \right)^S \right) \right) \quad [\text{cm}^2] \qquad (2.8)$$

Where LET_0 is the onset or threshold LET and width W and shape S are empirical fitting parameters.

It is difficult to obtain cross-section information for all incident angles during testing. Constraints on cost and time prevent collecting incident angle data, and often normal incidence events are used to calculate cross-section. To account for the directional dependence, two rate estimates for each device are calculated to bound the uncertainty: best-estimate, which is representative of realistic mean events, and worst-case, which incorporates margin and is recommended for design purposes. Best-estimate uses the Rectangular Parallel Piped (RPP) model to describe sensitive charge volumes in the device. When ionization from a particle exceeds the charge volume threshold, SEE is induced. RPP is a non-physical model that produces results following the cosine law up to angles of 60°. Best-estimate RPP dimensions are set to

43

equal width and depth values (X=Y), and height values one fifth the lateral (Z = X/5) [32].

Worst-case height is lower than best-estimate as it takes less charge to induce SEE, therefore producing larger upset rates. Worst-case is modeled to capture the unrestricted (*i.e.*, all angles) cosine-law where height approaches zero. Solvers do not typically tolerate charge volumes of 0, so an estimate of Z = X/100 is acceptable for capturing the limiting case [32]. The lateral dimension of the RPP model is found by taking the square-root of the saturated cross-section σ_{sat}. Best-estimate and worst-case are calculated for each environmental scenario. The output of this analysis shows the frequency of upsets per device in a given environment. Best-estimate and GCR is the most likely scenario in the matrix but are not guaranteed. For design purposes, it is recommended to use worst-case dimensions with the environment most representative of flight conditions (*e.g.*, missions during solar maximum should account for flare scenarios) [32].

2.2.5 Reliability Analysis

Low LET threshold and high upset rates do not explicitly disqualify a component. The final figure of merit required for thorough component performance evaluation is reliability, which captures the probability of success (or failure) for a given lifetime and orbit.

The exponential cumulative distribution function is used to determine reliability. The probability of failure is given by

$$F(t) = 1 - e^{-\lambda t} \tag{2.9}$$

And reliability given by

$$R(t) = 1 - F(t) \tag{2.10}$$

$$R(t) = e^{-\lambda t} \tag{2.11}$$

44
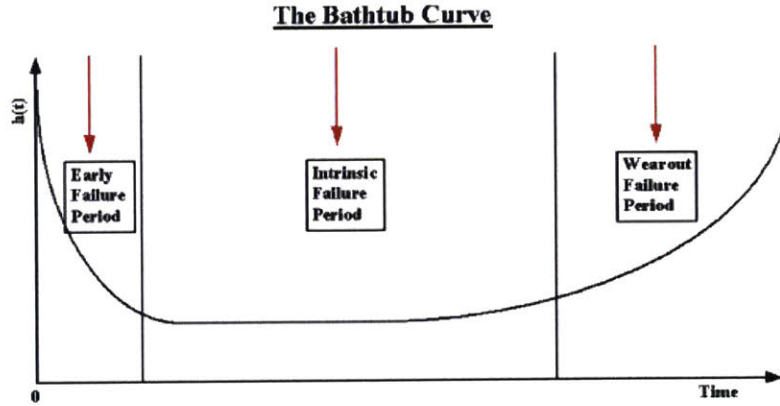
Figure 2-10: Bathtub curve illustrating the lifetime sections of a given component [44].

Where λ is the failure rate or upset rate and t is the mission lifetime.

Components having low probability of failure are low risk for a mission and may be used despite high upset rates or low LET thresholds. The failure rate of components due to SEE follows a bathtub curve (Figure 2-10) comprised of three key regions: first is infant mortality wherein failure decreases with time, second is useful life where the curve is approximately flat, and finally, the wearout life wherein the rate of failure increases with time [9].

2.3   OMERE Analyses for LEO Missions

Radiation effects are influenced by mission lifetime and orbit. To evaluate the LEO radiation environment and inform DC-DC converter radiation testing levels, analyses are conducted in OMERE for two proposed LEO constellation missions: Telesat Polar and Telesat Inclined, which are Walker constellations denoted by $i : t/p/f$, where i is the inclination of the orbital planes, t is the total number of satellites in the constellation, p is the number of constellation planes, and f is the number of "slots" between the first spacecraft in adjacent planes [59]. Table 2.3 summarizes the case studies. Telesat Polar is a Walker-Star 99.5°:91/7/1 constellation at 1000 km altitude with a 12-year mission lifetime. Telesat Inclined is a Walker-Delta 37.4°: 200/20/1 constellation at 1248 km altitude and same mission lifetime.

45

Table 2.3: Summary of LEO Constellation Mission from Telesat FCC Filing [18]

Orbit Name	Lifetime [years]	Altitude [km]	Inclination [°]
Telesat Inclined	12	1248	37.4
Telesat Polar		1000	99.5

Radiation environment modeling and subsequent analysis is performed in OMERE 5.2.2. Environment setup followed the standards recommended by the European Cooperation for Space Standardization (ECSS) E-ST-10-04 working group [16]. The trapped particle environment uses AP8 and AE8 models with Jensen Cain minimum and maximum magnetic fields, respectively. This represents the worst-case for both types of trapped particles. AP8 uses omnidirectional mean fluxes of protons with energy ranging from ~50 keV to 500 MeV while AE8 includes electrons with energy from ~50 keV to ~7 MeV [2].

Average statistical solar models use the Emission of Solar Protons (ESP) model [63] for solar proton fluence and the Predictions of Solar particle Yields for CHaracterizing Integrated Circuits (PSYCHIC) model [62] for heavy ion fluence. ESP is a computational approach to finding the percentile of the cumulative solar proton fluence distribution. It is built on the probability of exceeding a given fluence above an energy threshold for a given period. PSYCHIC extends this analysis to include heavy ions and extends the energy range to 300 MeV. This analysis used a 90% confidence level [16].

Solar flare activity is modeled with peak proton and heavy ion fluxes in varied time intervals to calculate upset rates. The worst-case 5-minutes scenario is used to incorporate margin in analysis. Other options include worst-case day and worst-case week, though this is not an exhaustive list. The CREME-96 model [61] is used for in-flare protons and heavy ions.

GCR models use GCR ISO 15390 [46] to calculate the proton and heavy ion flux and fluence contributions from cosmic rays. In conjunction with a quiet magnetic field configuration, this model represents a worst-case for GCR activity.

Total ionizing dose, or dose depth curve, is calculated using the Shieldose-2 model [57] with a solid sphere configuration which assumes a Silicon target centered in a
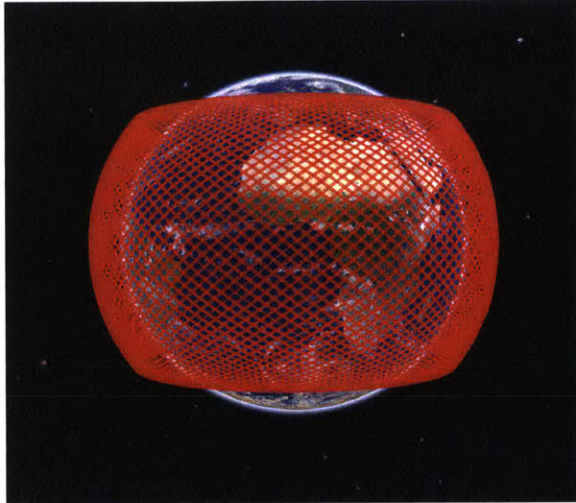
(a) Telesat Inclined Constellation generated in OMERE 5.2.2. The constellation is a Walker-Delta configuration with a 37.4° inclination and 1248 km altitude.
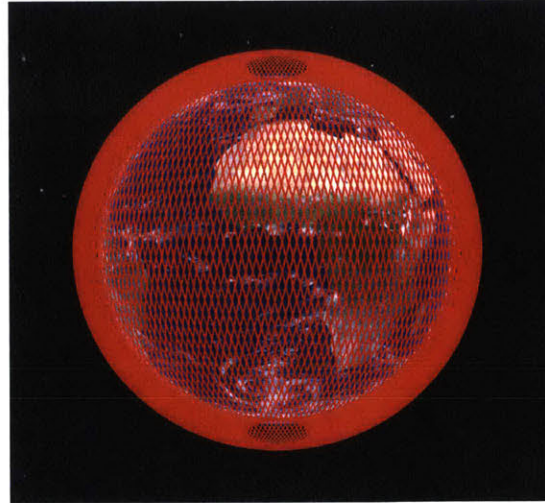
(b) Telesat Polar Constellation generated in OMERE 5.2.2. The constellation is a Walker-Star configuration with a 99.5° inclination and 1000 km altitude.

Figure 2-11: Each constellation has a 10-year operational lifetime with 2 years of in-orbit storage. The simulation start date is set for January 1, 2022 [18].

sphere with varying shielding thickness in the radial direction and omnidirectional radiation exposure. This model typically over-estimates total dose because the integrated target is additionally shielded by the spacecraft and is not irradiated equally in all directions. Figure 2-12 shows the dose-depth curve for both Telesat Polar and Inclined orbits. Note the inclined orbit receives an overall higher dose due to spacecraft orbiting in areas of higher trapped particle flux. Increasing shielding to decrease dose is effective up to ~300 mils, but quickly results in diminishing returns.

Displacement damage curves are generated assuming normal incidence particles and a target material of Silicon which illustrate the amount of non-ionization energy per unit mass is absorbed as a function of shielding thickness. For testing applications, equivalent fluence may be used to induce an equivalent level of displacement damage with a mono-energetic particle, in this case, 10 MeV protons. Figure 2-13 shows the displacement damage dose depth curve and equivalent fluence curve.

Figure 2-14 captures the expected flux spectrum as a function of LET for each orbit given a shielding thickness. Integral particle flux describes the total particle flux for all species between zero and a given energy level. Plotted against LET, integral
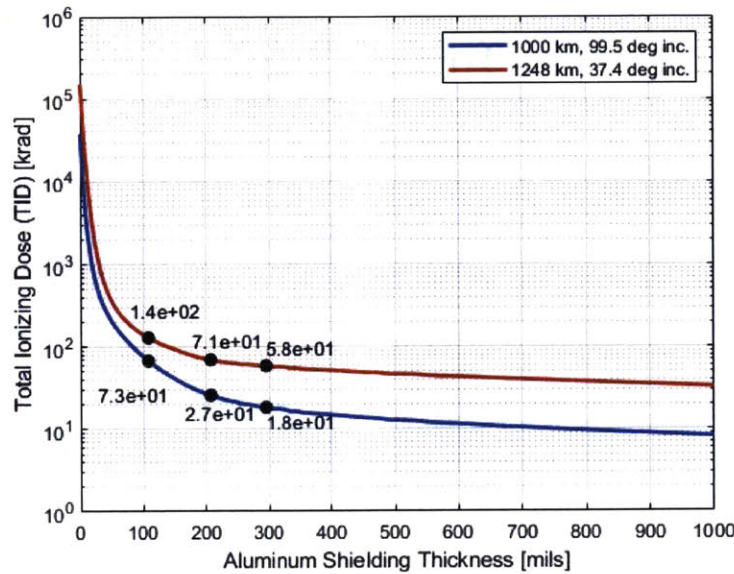
Figure 2-12: Total Ionizing Dose as a function of shielding thickness. Values at 100 mils (2.54 mm), 200mils (5.08 mm), and 300 mils (7.62 mm) are marked.

flux in a target material of Silicon shows the total charged particle flux for a given energy transfer. A threshold flux of 10^{-7} is selected, as particle flux below this level is negligible. The intersection of the integral flux curves and the threshold value reveals the highest expected LET value for each configuration.

The results from each analysis are summarized in Table 2.4. Using 200 mils of Aluminum shielding as a baseline, the maximum values between the two orbits established testing levels. The maximum LET value from each case study orbit assumes omnidirectional fluxes. During testing, this can be addressed in two ways: the first is testing devices at angle, which is often not feasible due to time and budget constraints. The second is determining the equivalent normal incidence LET for a particle that strikes at a maximum angle of 60° (i.e., apply the cosine law). In summary, components should be TID tested to at least 71 krad (Si) and SEE tested to an LET of 63 MeV-cm^2-mg^{-1}.

Table 2.4: Radiation Analyses Summary for Telesat Constellations

Orbit	Telesat Polar 1000 km, 99.5°			Telesat Inclined 1248 km, 37.4°		
Shielding [mils(Al)]	100	200	300	100	200	300
TID [krad(Si)]	73	27	18	140	71	58
DD [MeV-g^{-1}]	7.2×10^8	4.9×10^8	4.0×10^8	2.0×10^9	1.5×10^9	1.3×10^9
Min. Onset LET [MeV-cm^2-mg^{-1}]	37.5	31.1	30.7	2.07	2.12	2.22
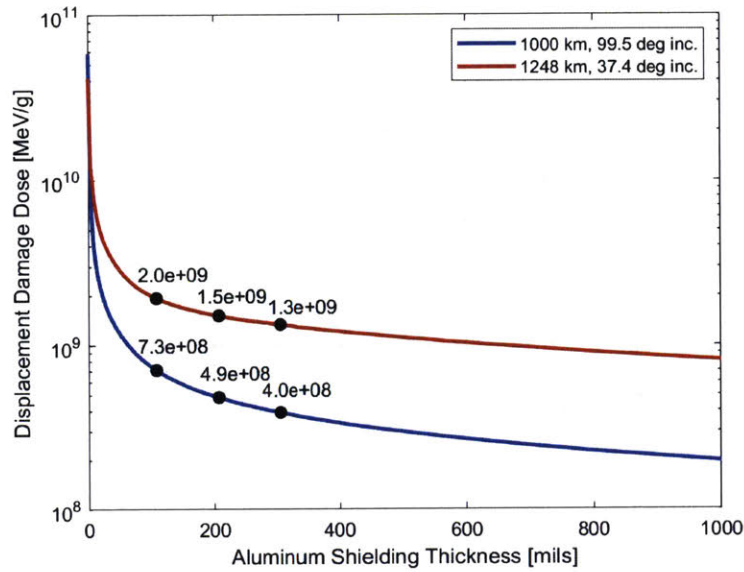
(a) Displacement Damage Dose Curve
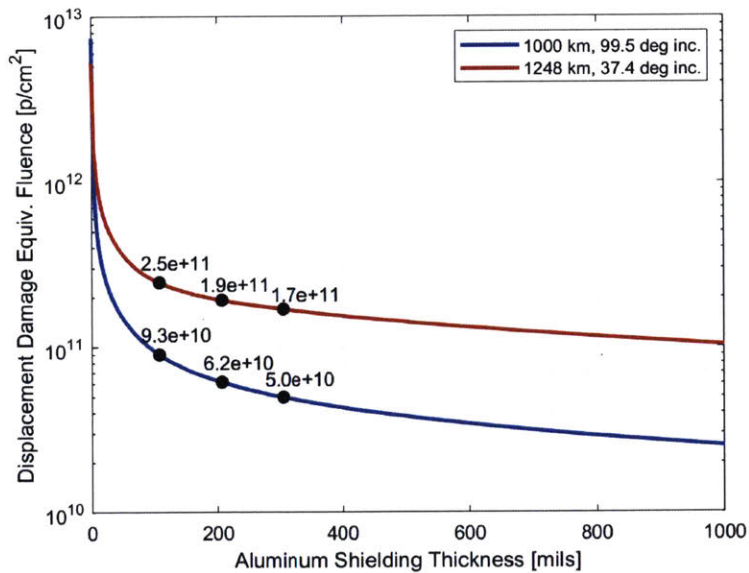
(b) Equivalent Fluence Curve for 10 MeV Protons

Figure 2-13: Displacement Damage Dose Analysis from OMERE 5.2.2. Displacement damage dose is analogous to total dose depth and captures the amount of non-ionizing damage in Silicon for a given shielding thickness. Equivalent fluence is useful for testing purposes and may be used to determine the total number of mono-energetic particles needed to induce the same level non-ionizing damage.
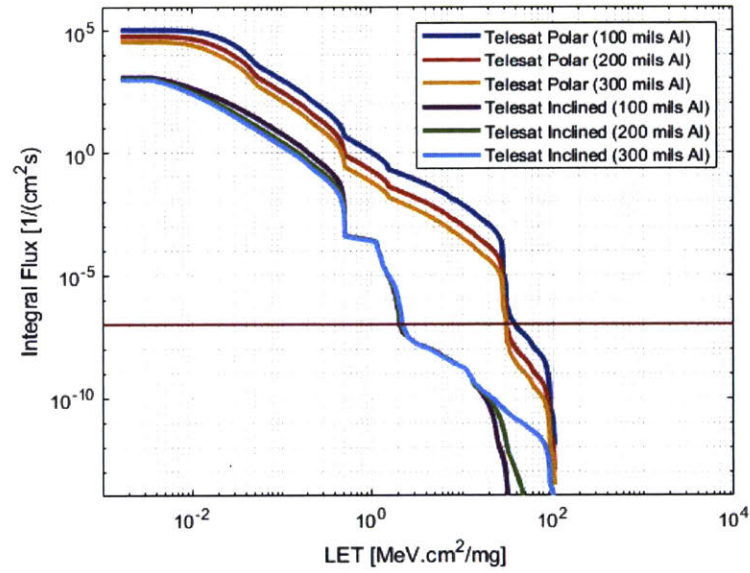
Figure 2-14: Integral flux spectrum for reference cases in the LEO radiation environment.

Chapter 3

TID and SEE Experiments

Three different commercial step-down DC-DC converters are characterized for space applications through TID and SEE testing. The radiation environment analysis presented in Chapter 2 informs testing levels, and implementation of these levels are discussed here. The parts to be tested are PowerSoC switched step-down (buck) converters with an integrated inductor and control IC in the same package. Table 3.1 summarizes nominal operating conditions for each part. The characteristic discrepancy between these devices are the supported loads (I_{out}). These components will be referred to as the 4A, 8A, and 12A devices. We note the 4A device has a Light Load Mode to support output currents less than 100 mA at increased efficiency, and the 8A and 12A devices may be configured in a master-slave architecture. For brevity, these additional modes are not investigated, and stand-alone, nominal operation modes are used during experiments.

Table 3.1: Nominal operating conditions and parameters for tested DC-DC converters

Max I_{out} [A]	V_{in} Range [V]	V_{out} Range [V]	Package Size [mm]
4	2.5−6.6	0.75−VIN	QFN38 (4 × 7)
8	2.5−6.6	0.6−VIN	QFN68 (8 × 11)
12	2.5−6.6	0.6−VIN	QFN76 (10 × 11)

Evaluation boards provided by the manufacturer are used during both tests. Access to key parameters is not inhibited by the evaluation board setup and no custom PCB with additional probe points is required.

3.1 Total Ionizing Dose (TID) Testing

In this section, the TID test and relevant electronics configuration is described. The test results are in Chapter 4. Testing levels are guided by the analysis performed in Chapter 2 of this thesis, and by MIL-STD-883 used by the military and aerospace industry to qualify parts suitable for respective applications [29].

Testing is performed at Air Force Research Laboratory with JD Instruments, in Albuquerque, New Mexico. The devices are exposed to a gamma ray source in a Cobalt-60 chamber. In accordance with MIL-STD-883 1019.4 Condition A, each set of parts are exposed to a Cobalt-60 source with an applied high dose rate of 62 rad/s to a cumulative dose of 100 krad(Si). The first three devices are step-wise irradiated to levels of 10k, 25k, 50k, 75k, and 100k rad(Si). This acted as a coarse irradiation to determine parametric sensitivity to dose. The second set is irradiated at 40k, 50k, 60k, 70k, 80k, and 90k rad(Si). This fine irradiation is used on the second set of parts to better understand failure thresholds of the devices.

3.1.1 Test Parameters

The following parameters are monitored during total dose testing and subsequent justification provided: Input Current and Output Voltage vs. Dose: using a known load and controlled power (voltage) supply, these values are used to determine converter efficiency vs. dose. The difference between the input and output power can be attributed to radiation-induced defects impacting component performance. Additionally, the output voltage measurement will reveal if the device is susceptible to parametric shifts, and if so, the sensitivity of shifts to dose. Three load conditions are tested to screen for cumulative radiation-induced defects:

1. High load, wherein the output current is near the maximum rated device current.

2. Light (small) load, wherein the output current is within the operating specifications of the device.

3. No load, wherein there is no output current and additional current draw, referenced to the control device, is attributed to radiation-induced defects such as leakage current.

Output Voltage Transients vs. Dose: observing the response of the system as the load conditions change provides insight into the onboard control functionality and the radiation-induced defects to inaccessible parts of the PowerSoC.

3.1.2   Board Configuration

A total of 6 components are subdivided into 2 sets with 1 device type per set (total 3 per set) for testing. The goal of this experiment is not to perform lot screening; however, sufficient statistics are needed to qualify these parts for space applications, which motivates testing greater than one device of each type. Converters are biased with 5 V input with a fixed 3 V, output analogous to flight conditions. A total of three test modes are used to measure radiation-induced degradation: full load, light load, and no-load conditions. Each test mode has a corresponding resistor load that is manually switched during irradiation, as summarized in Table 3.2. Figure 3-1 depicts the switched load board architecture used to induce transients and vary output current conditions. No spot shielding on the evaluation board is required because no other active components are present.

Table 3.2: TID Test Electrical Configuration. All devices are tested under bias. A total of 3 loading conditions are tested to determine parameter shifts as a function of total dose.

Test Mode	Full Load			Light Load			No Load		
Device	4A	8A	12A	4A	8A	12A	4A	8A	12A
Total Resistance [Ω]	0.88	0.47	0.32	39	39	39	—	—	—
Output Voltage [V]	2.94	2.87	2.82	2.94	2.87	2.82	2.94	2.87	2.82
Input Voltage [V]	5	5	5	5	5	5	5	5	5
Output Current [A]	3.341	6.106	8.813	0.075	0.074	0.072	—	—	—
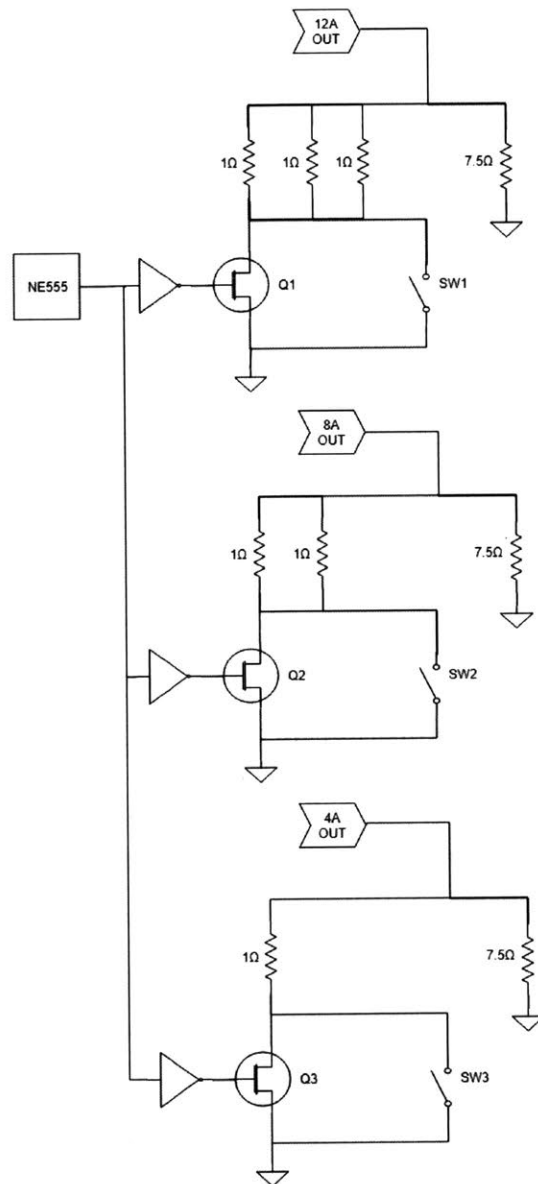
Figure 3-1: Simplified layout of the load board used to induce Full Load (high current) conditions. The 555-timer is set to a 2.86% (400s/14ms) duty cycle. The output is inverted and applied to the gate of a NFET, which would momentarily connect the resistor network to ground, drawing higher currents from the DUTs. This mode is used to observe transient responses as a function of dose. The switch can be enabled manually, and is used to observe total high current draw and calculate conversion efficiency as a function of dose.
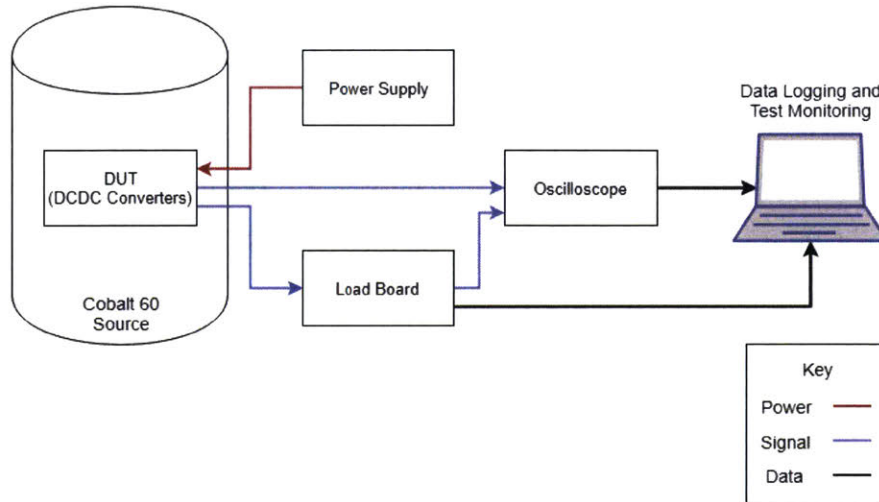
Figure 3-2: TID Test Setup. The converters are exposed to gamma radiation in the Cobalt-60 source while other sensitive electronics, such as the load boards, power supplies, and monitoring hardware, are located outside the irradiation chamber.

3.1.3 TID Levels and Test Setup

Only the DUTs are exposed to the Cobalt-60 source. The load board, power supply, monitoring and data logging hardware are located and controlled remotely. Figure 3-2 illustrates the test setup. After the desired radiation levels are achieved, each device is:

1. Power cycled

2. Forced high current state to observe voltage transients and input currents for efficiency calculations

3. Forced no-load state to record input currents for leakage currents

4. Forced light-load state to record input currents for leakage currents and efficiency calculations

After exposure, the device annealed at room-temperature for 24 hours (8A and 12A) and 72 hours (4A). All devices regained functionality after annealing showing high TID tolerance.

57

3.2 Single Event Effects (SEE) Testing

In this section, we describe the SEE test and relevant electronics configuration. The results from this testing are discussed in Chapter 4. Testing is guided by analysis performed in Chapter 2 and by JEDEC standard EIA/JESD57, which is developed by the US Government RHA subcommittee and used as the industry standard for electronics SEE screening [39]. The goal of this test is to determine device cross section vs. LET for relevant effects and to characterize transient response if applicable. Analog devices are screened for Single Event Latchup (SEL) and Single Event Transient (SET) effects. SEL is defined as an abnormal high current state due to parasitic BJT activation by an energetic particle resulting in the loss of device functionality [30]. SEL may or may not be destructive (*i.e.*, the device may return to nominal operation or exhibit a persistent failure mode after power cycling). SET is defined as a momentary voltage excursion at a node caused by an energetic particle [30]. Both types of events have potential to negatively impact the larger system or spacecraft and it is critical to understand the device response to quantify risk. Heavy ion testing is performed at Brookhaven National Laboratory (BNL), NASA Space Radiation Laboratory (NSRL). Ions from Brookhavens Booster accelerator are used to test the converters in air. The ions meet the LET of 60 MeV-cm^2-mg^{-1} level derived in Chapter 2 and provide sufficient range through the part including plastic packaging. This is not the case for all heavy ion facilities, and electronics can require the removal of the plastic top (*i.e.*, de-lidding) when ions have relatively low initial energy.

3.2.1 Test Parameters

The following parameters are monitored during heavy ion irradiation: Temperature: in accordance with JESD57, SEL screening requires thermally stressing the DUT [29]. A thermocouple and thermometer read out the device temperature during irradiation, and a heat gun is modulated based on the feedback to maintain a device temperature of 85°C ± 5°C. Input voltage and input current: dynamic or anomalous behavior may indicate SEE. Output voltage and input current: dynamic or anomalous behavior may

Ion Species [1]	Max Energy [2] (MeV/n)	LET in Si at Max Energy [6] (MeV/(mg/cm^2))	Peak LET in Si (MeV/(mg/cm^2))	Range in Si (mm)	Max Flux [3] (ions/spill)
H^1	2500	0.00171	0.51	5470	2.2×10^{11}
He^3	1500	0.006679	1.5	2220	0.88×10^{10}
He^4	1500	0.006919	1.5	2960	0.88×10^{10}
Li^7	1500	0.01557	2.3	2274	4×10^9
C^{12}	1500	0.06227	5.2	972	1.2×10^{10}
O^{16}	1500	0.1107	7.3	729	0.4×10^{10}
Ne^{20}	1500	0.173	9	583	1.2×10^{10}
Si^{28}	1500	0.339	14	417	0.3×10^{10}
Cl^{35}	1500	0.4999	17.4	353	0.2×10^{10}
Ar^{40}	1500	0.5605	18.7	360	0.02×10^{10}
Ti^{48}	1500	0.8372	24.2	289	0.08×10^{10}
Fe^{56}	1470	1.171	29.3	235	0.2×10^{10}
Kr^{84}	383	3.28	41	26.5	2.0×10^7
Zr^{91}	300	4.58	48.5	15.6	1×10^6
Nb^{93}	300	4.8	47.4	15.4	1×10^6
Xe^{132}	350	7.7	69.2	16.3	5.0×10^7
Ta^{181}	342	14.8	87.5	12.1	3.0×10^8
Au^{197}	165	24.7	94.2	3.7	1.0×10^8
Th^{232}	217	25.0	107	5.7	1×10^7

Figure 3-3: Ions and Energies for Electronics Testing Provided by NSRL [12].

indicate SEE. Power OK (POK) signal: dynamic or anomalous behavior may indicate SEE.

3.2.2 Board Configuration

Evaluation boards provided by the manufacturer are used for SEE testing. At least 2 devices and at most 3 devices from each converter type are tested to screen for manufacturing variability, though lot screening is not considered for this test. Each board is biased with a 5.5 V input and fixed 3 V output.

3.2.3 Ion Selection

NSRL users have access to a suite of ion types and energies to perform SEE screening. Figure 3-3 shows a breakdown of the available ions and energy ranges.

Heavy ion facility time is charged hourly so maximizing test time (minimizing setup time) is desirable. Each ion has an associated setup and calibration time overhead so 2-3 ions at most are used for screening.

Ions are selected based on a target LET in the DUT, which is 60 MeV-cm^2-mg^{-1} at normal incidence in a target material of Silicon for this experiment. Figure 3-3 shows the ions meeting this criterion are Xeon, Tantalum, and Gold. A full SRIM analysis is required to inform final selection.

LET of ions in a medium follows a Bragg curve, which peaks some distance from initial entry, meaning ions must be nearly stopped along-track to reach relatively high LET values. If the ion initial energy is low, air acts as a degrader material to stop the ion, and the desired LET level is achieved by positioning the DUT at a known distance from the beam aperture. The initial energy of the NSRL ions is high enough such that additional degrader is required to reach relatively high LET values. NSRL provides binary high-density polyethylene (HDPE) filters that can be placed in front of the DUT in the beamline to tune LET. The HPDE degraders range from 0.25 mm to 255.75 mm, allowing users to select thicknesses in 0.25 mm steps for a total thickness of 20.831 cm. NSRL provides LET vs. HDPE degrader thickness curves for users to determine the amount of desired degrader to achieve a target LET, however, the DUTs are not de-lidded (*i.e.*, die are still shrouded in plastic packaging), so additional analysis is performed to account for the package thickness preceding the die. Each die had slightly different cap thicknesses and the SRIM analysis for the 4A part is shown as an example.

The SRIM analysis for Xeon, Tantalum, and Gold reveals two viable combinations to produce a desired LET spectrum: Xenon and Gold or Tantalum and Gold. Note the initial energies used in the SRIM analysis differ from the NSRL tables, because upon receiving test confirmation, NSRL provided actual energies that would be used for this setup. Ultimately, Tantalum and Gold are selected for testing because Tantalum offers better linearity in the target range (*i.e.*, 20-60 MeV-cm^2-mg^{-1}). SEE screening requires different fluence levels for different effects. In accordance with the EIA/JESD57 standard, SET screening requires minimum fluence levels of 10^6
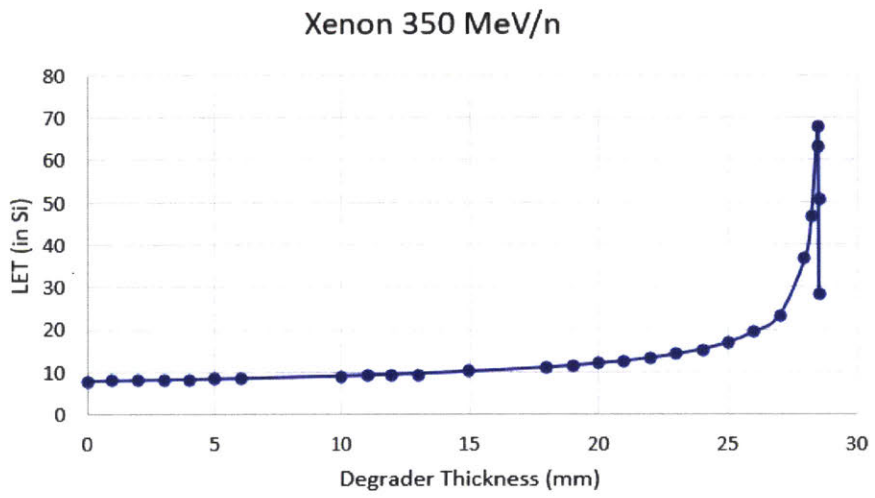
Figure 3-4: Calculated Xenon Bragg curve for target material of Silicon and initial energy.
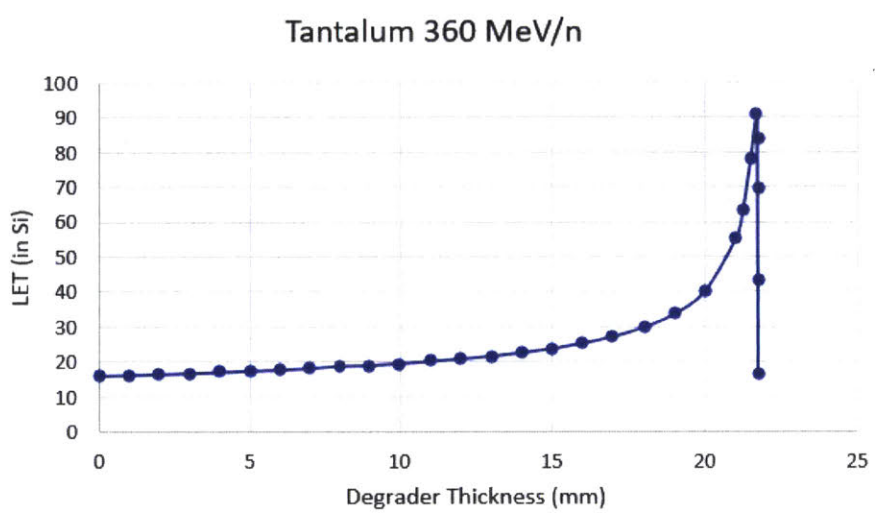
Figure 3-5: Calculated Tantalum Bragg curve for target material of Silicon and initial energy.
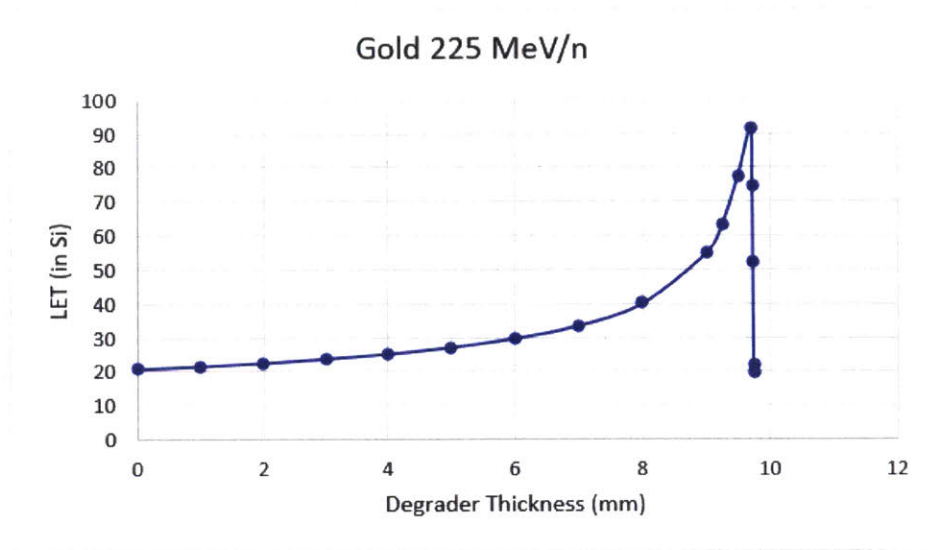
Figure 3-6: Calculated Gold Bragg curve for target material of Silicon and initial energy.

ions/cm^2 or ≥ 100 events and SEL screening requires 10^7 ions/cm^2. For each test, the DUT maintained a temperature of 85°C $\pm$ 5°C. Table 3.3 summarizes the test conditions for each SEE screening

Table 3.3: SEE Test Conditions

SEE Type	SEL	SET
DUT Temp	85° C	85° C
Fluence	10^7 ions/cm^2	10^7 ions/cm^2 or $25-32$ events
Load	1A	1A
Oscilloscope Trigger Level	N/A	$\pm$ 200 mV on Channel A set to the 1 V$_{pp}$ vertical scale and AC coupled OR the power OK signal falling below 4 V on Channel C set to the 10 V$_{pp}$ vertical scale and DC coupled

3.2.4 Test Setup

The evaluation board is placed on the beamline, and the beam is focused such that only the DUT is irradiated (e.g., to a 4×7 mm^2 incident area for the 4A device). The board is positioned for ion normal incidence and remains static for the duration of the
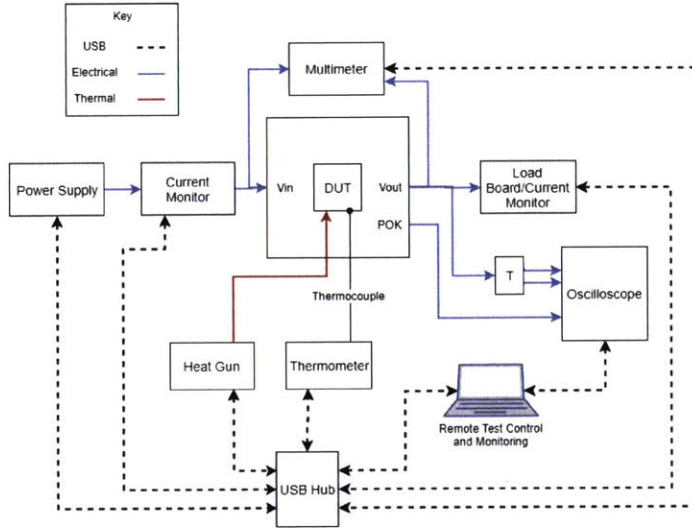
Figure 3-7: Block diagram of the SEE test setup. The DUT input voltage and current, output voltage and current, and temperature are monitored remotely during testing.

experiment. Electrical support equipment including power supplies and monitoring hardware are co-located in the beam room to minimize noise introduced to measured signals but are off the beamline axis and shielded with lead for additional protection. The electrical equipment and monitoring hardware are controlled remote via USB connection through a USB hub connected to a PC located in the operations room (outside of the target room). Figure 3-7 shows a block diagram of the test setup to monitor test parameters. The power supply provides the required 5.5 V input bias, and the current monitor preceding the input monitored the current draw. The multimeter reads out the input and output voltages, and the oscilloscope plots both the output voltage and POK signal for transient events. V_{out} is AC coupled and triggers on $\pm$ 200 mV changes; POK is DC coupled and triggers on the signal falling below 4 V. The load board had an integrated current monitor to track to the output current.
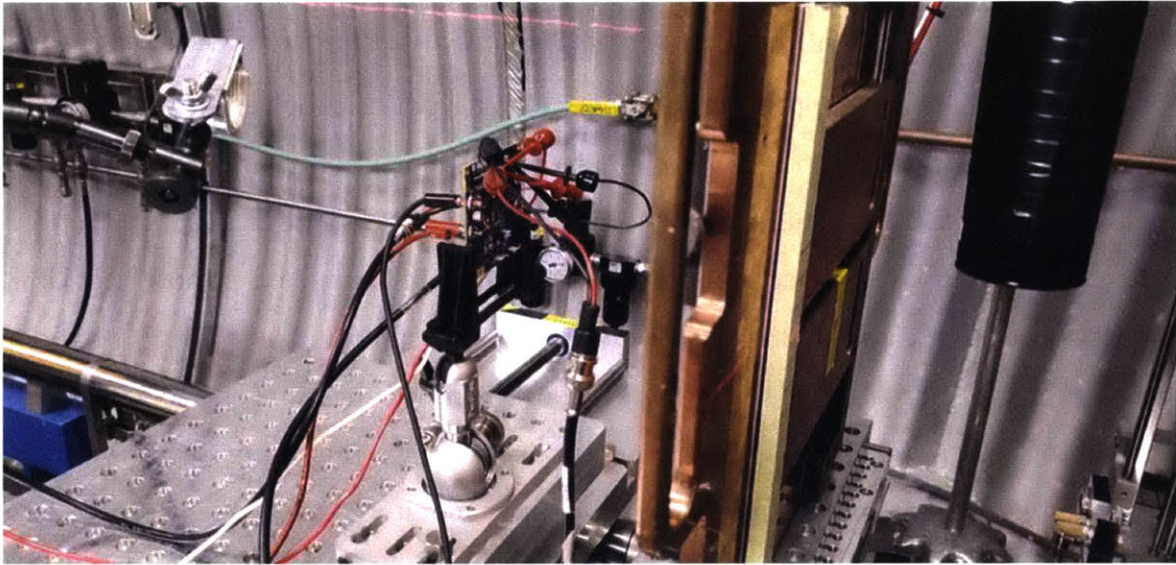
Figure 3-8: Evaluation board on the NSRL beam line during SEE testing

Chapter 4

Results

Three commercial-grade step-down converters were tested for TID and SEE effects. Testing revealed these devices exhibit varying levels of sensitivity to radiation across all testing.

4.1 TID Results

All DC-DC converters experienced a failure mode during TID testing with different failure thresholds. The 4A device failed between 60 and 70 krad(Si). The 8A and 12A devices showed similar dose sensitivity failed between 90 and 100 krad(Si). The device failure mode was inability to restart after power cycling following an irradiation step. Across all parameters, the 4A device showed highest sensitivity and the 8A and 12A devices responded similarly to dose. Figure 4-1 shows the measured output voltage vs. dose, with 4A having the highest variation.

While it is desirable to measure leakage current, the device complexity and decision to use the commercial evaluation board prohibited direct measurements of leakage current. Instead, input current levels across dose for three load conditions were measured, and output current from the load condition was calculated. Finally, input power and output power were calculated and compared to find efficiency. Deviation from the efficiency calculated at 0 krad(Si) indicates damage, and drops in efficiency can be used as a proxy for leakage current.
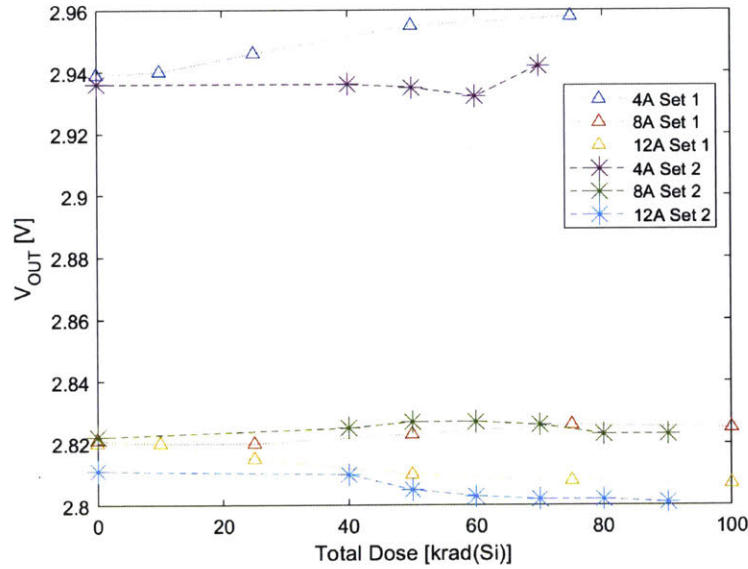
Figure 4-1: Output Voltage vs Dose. The 4A device exhibits highest sensitivity to radiation, showing the largest output shift (19 mV in set 1).

Figures 4-2 through 4-4 show the input current across tests and dose. No load input current and light load input current exhibited approximately equal sensitivity to dose ($\sim$150 mA maximum change, 12A part), while full load was the lowest ($\sim$ 10 mA maximum change, 12A part). While these values were not strictly used as a performance gauge, they give insight to the part response.

During light load testing, efficiency decrease is seen across all devices. The 4A device efficiency decreases most between 50 and 60 krad(Si), which immediately precedes the device failure threshold. The 8A and 12A show efficiency decline between 60 and 80 krad(Si) also immediately preceding failure. This behavior is expected as lower efficiency may point toward increased leakage current (increased input current) or operating parameter shifts (increased power dissipation) inducing a failure state.

The high current state exhibits unexpected behavior as the efficiency increases for both sets of 4A and 8A devices. An explanation for this could be that the integrated control circuitry is intervening by shutting down superfluous processes or modulating the switching frequency differently, reducing the power losses to peripheral power conversion processes. Figures 4-2 and 4-5 show efficiency across tests and dose.

The final parameter monitored during TID testing was transient levels. Output

66
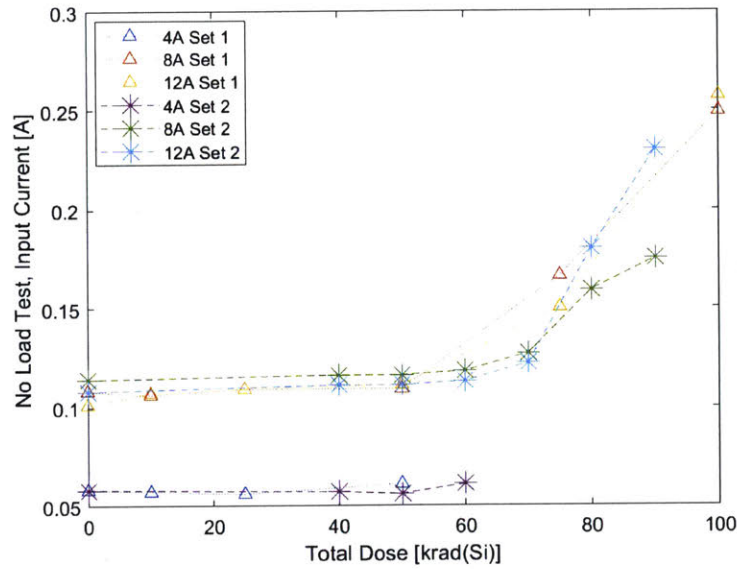
Figure 4-2: Input Current vs. Dose for No Load Testing. The 8A and 12A part show highest sensitivity, and input current increase is seen between 50 and 60 krad(Si).
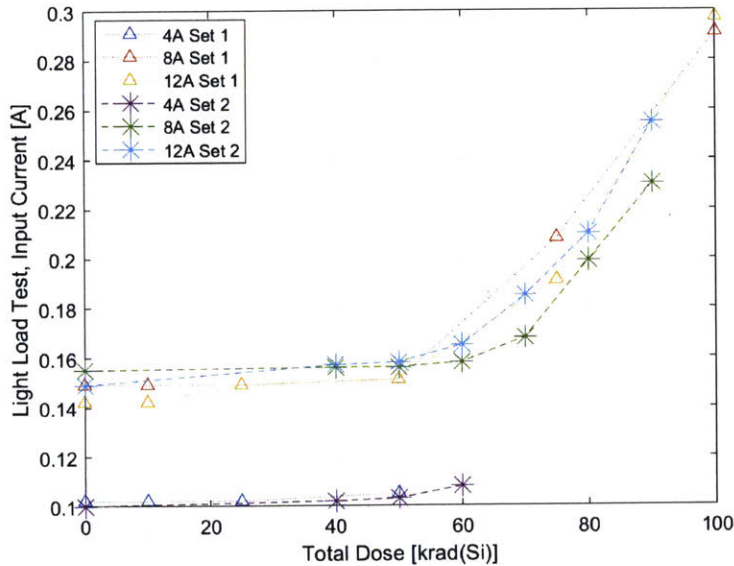
Figure 4-3: Input Current vs. Dose for Light Load Testing. The 8A and 12A part show highest sensitivity, and input current increase is seen between 50 and 60 krad(Si)

voltage transients were captured by a remotely located oscilloscope and induced by a NE555 timer. The output signal was AC coupled and varied with dose. Figures 4-7 through 4-9 show oscilloscope screen captures of the 8A output as at 40, 70, and 80 krad(Si). The magnitude of the transient is reduced after a dose threshold, which is between 70 and 80 krad(Si) for this device. Gain reduction potentially supports
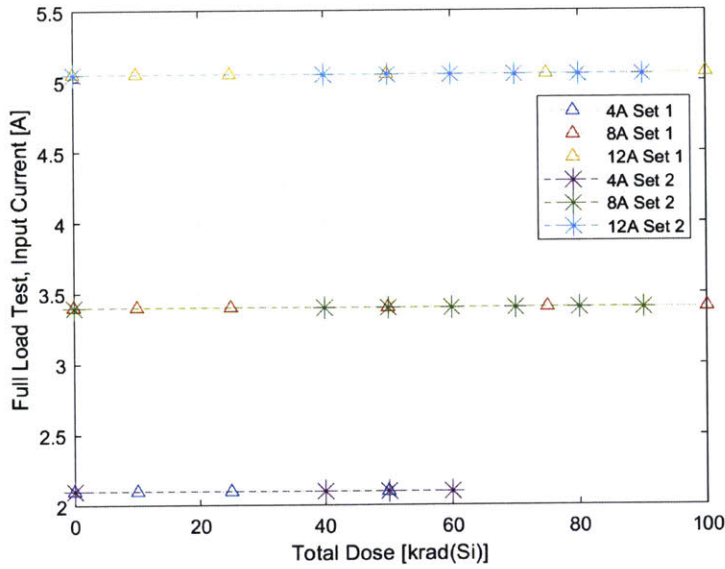
Figure 4-4: Input Current vs Dose for Full Load Testing. None of the devices exhibited sensitivity in this test mode
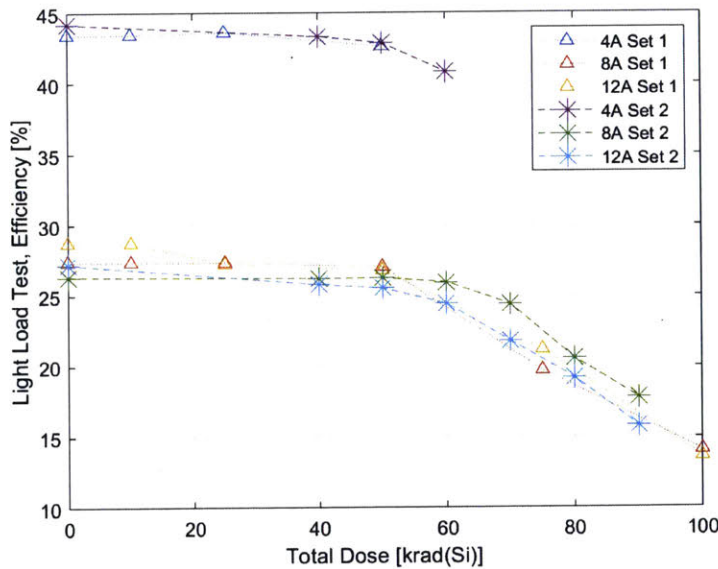
Figure 4-5: Efficiency vs Dose for Light Load Testing. Decreases in efficiency precede failure thresholds. The 4A device begins decreasing in efficiency around 50 krad(Si). The 8A and 12A devices begin decreasing around 60 and 70 krad(Si).

the hypothesis of intervening control circuitry. Output voltage is is a function of switching frequency [23]; by reducing the switching frequency, less power is required to operate the device and an increase in efficiency is possible. This is speculation and additional testing is required to conclusively determine the underlying cause of the
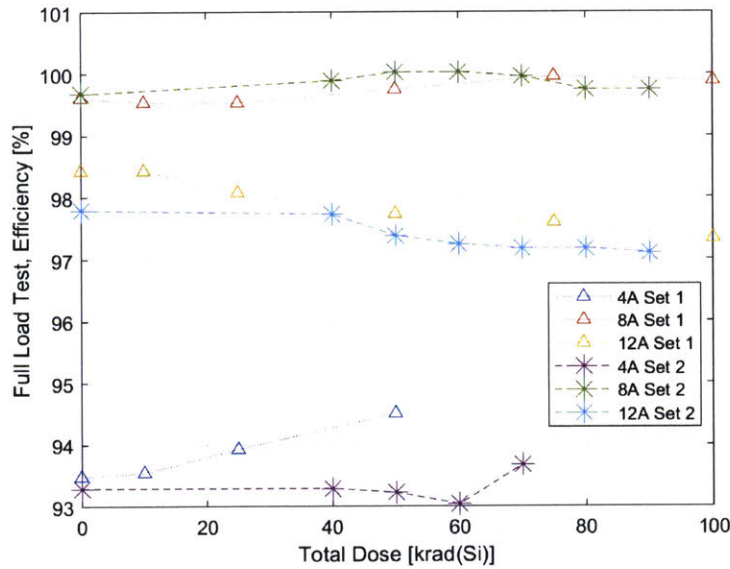
Figure 4-6: Efficiency vs Dose for Full Load Testing. The 4A and 8A devices exhibit increases in efficiency. This is potentially caused by control circuit intervention and internal regulation.

devices radiation response.
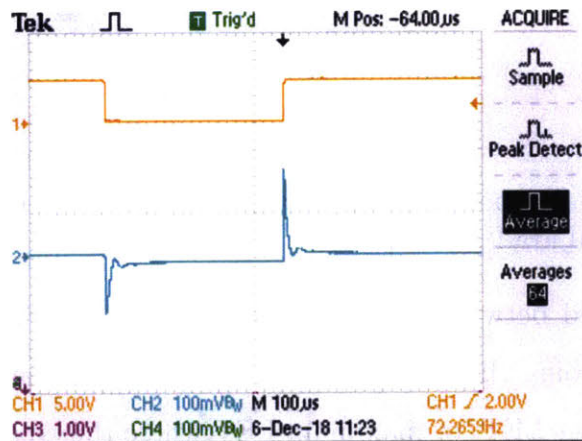
Figure 4-7: Transient Response of 8A device at 40 krad(Si).

4.2 SEE Test Results

All converters were latch-up free to the maximum experimental LET. SET was observed across all devices with varied magnitude and duration. Single Event Functional Interrupts (SEFIs), defined as a non-destructive interruption causing the device to reset, were also observed on the 8A and 12A devices. No significant deviations in

69
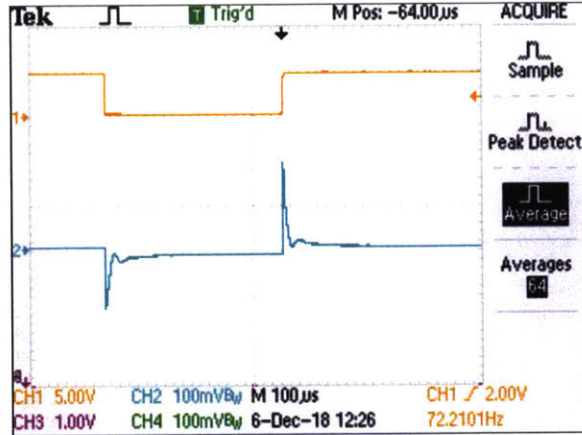
Figure 4-8: Transient Response of 8A device at 70 krad(Si). Output is similar to 40 krad(Si) output.
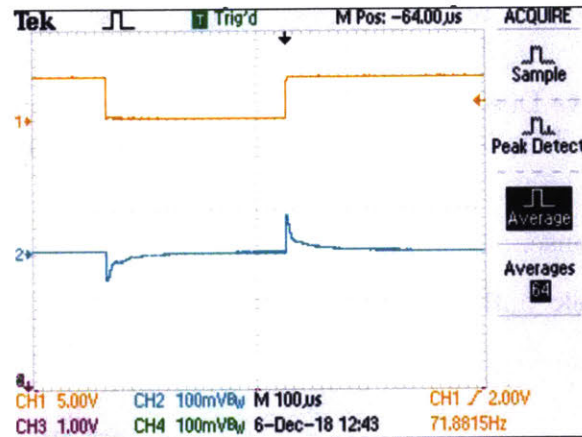
Figure 4-9: Transient Response of 8A device at 80 krad(Si). Output is reduced compared to 40 and 70 krad(Si) response.

behavior were observed between device samples or load conditions. Recall Eq. 2.8 from Chapter 2 describing the Weibull fit, where σ_{sat} is the saturation cross-section value, LET_0 is the onset LET, or maximum LET where the cross-section is zero, and S and W are empirical shape and width parameters, respectively. A discussion on Weibull curves and empirical parameters is provided in Chapter 2.

A total of four distinct events are seen across parts and binned as SET or SEFI. Persistent shutdowns exhibited simultaneous voltage drops on V_{out} and POK. Signals fell to zero volts and remained in the off state until power cycled externally. Shutdowns with restart showed similar behavior, but instead of remaining off until externally power cycled, the device spontaneously attempted to recover until successfully restarting. Transient shutdowns also saw POK and V_{out} signals drop to zero

70
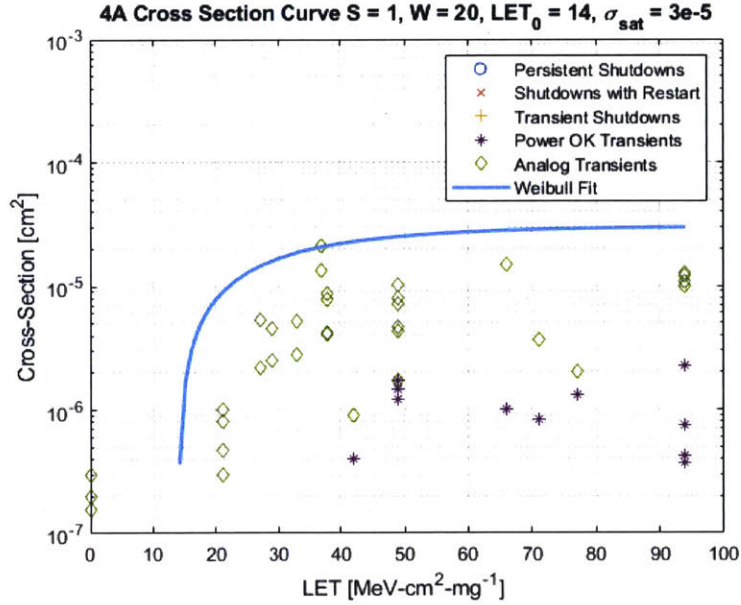
Figure 4-10: 4A Cross Section with S = 1 and W = 20. The onset LET is 14 MeV-cm^2-mg^{-1} and saturates at 3E-5 cm^2.

volts, but instead of multiple recovery attempts, the device would turn on a few milliseconds after initial shutdown. The final event was analog transient, wherein V_{out} and POK oscillated for a few milliseconds before returning to nominal levels. All shutdown events are classified as SEFIs, and analog transients are SETs.

The cross-section curves for each device are found in Figures 4-10, 4-12, and 4-14. The minimum onset LET for all devices is 14 MeV-cm^2-mg^{-1}. While this is below the LET requirement derived in Chapter 2, further analysis reveals these devices have low upset rates and low probability of failure, making them viable candidates for space applications. Additionally, the lack of destructive events implies a SEE can be mitigated without risking system upset or system failure. Events were recorded for a calculated LET of 0. This is an artifact of imperfect SRIM models (*e.g.* material approximations and uniform mass distributions) and uncertainty in beam distribution (*e.g.* path of particles). The actual LET of events recorded at 0 are between 14 and 92 MeV-cm^2-mg^{-1}.

The 4A device experienced analog transients on V_{out} (Analog Transients) and on POK (Power OK Transients) and no shutdown events. Note the cross-section for POK events is different relative to Analog Transients and a separate curve may be

71

generated for those events.

For this thesis, a separate curve was not generated because every POK Transient corresponded to an Analog Transient event contributing to the Analog Transient cross-section. Device performance and upset rates will thus be dominated by the Analog Transient cross-section as it has a higher saturation and lower cross-section.

No SEFIs were seen on any samples of this device across all LET. The highest cross-section saturation is seen on the 4A device indicating this device experienced the largest number of events during testing. Figure 4-11 displays oscilloscope outputs of both types of events. The maximum duration of a transient event was 8 us. The nature of the transient was to ring or oscillate on V_{out} with a maximum amplitude of 2.31 V and minimum of 1.78 V.
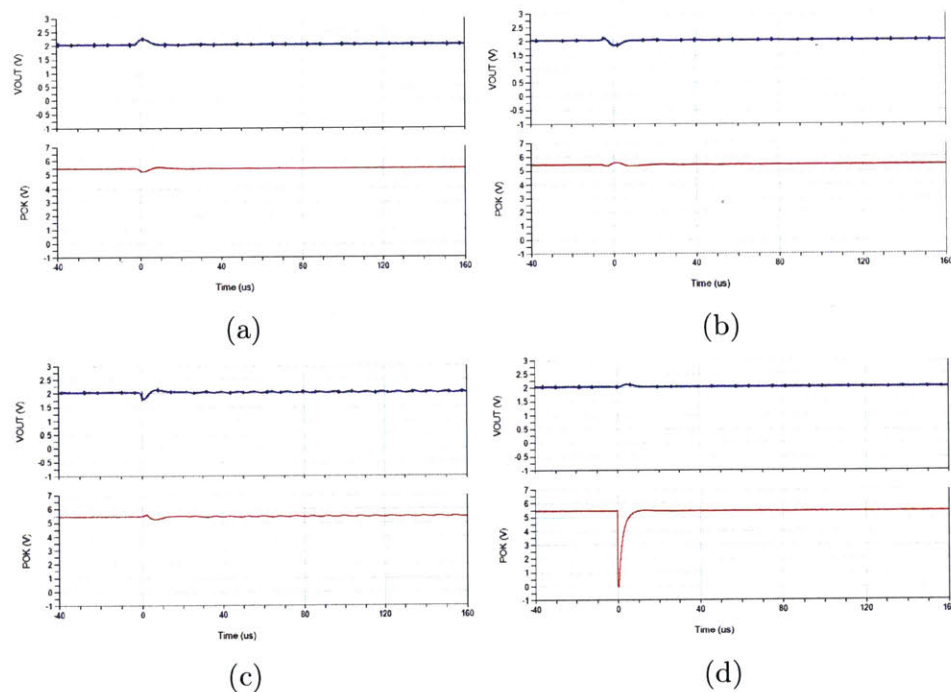
Figure 4-11: Transient events observed on the 4A Device. a-c shos oscillations on V_{out}, and D shows transients on POK.

The 8A device exhibited SET and SEFI behavior across all samples and LET. All events have the same cross-section, and thus one Weibull curve was generated. The maximum time recorded for a POK event was 593 ms, however this is not reflective of true transient behavior as this corresponded to a SEFI (*i.e.*, required external power

72
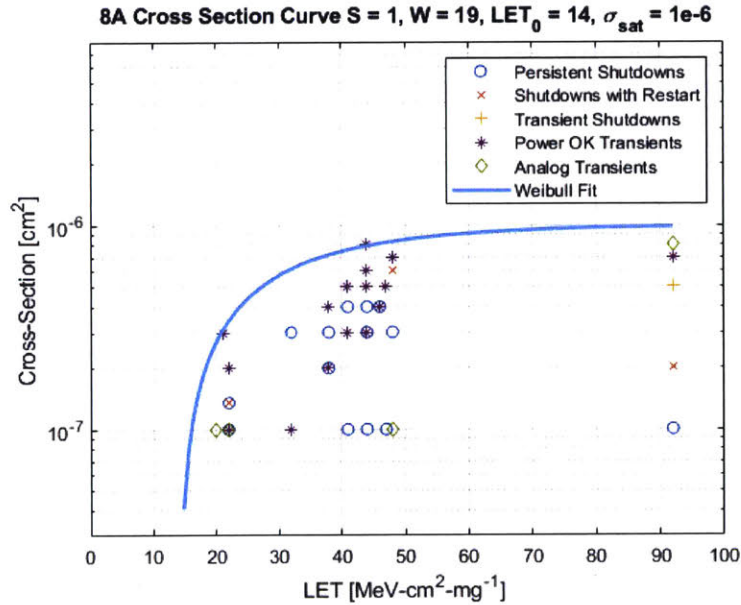
Figure 4-12: 8A Cross Section with S = 1 and W = 19. The onset LET is 14 MeV-cm^2-mg^{-1} and saturates at 1E-6 cm^2.

cycling). Typical POK and V_{out} transients lasted a few milliseconds. The maximum amplitude of a transient was 2.3 V and minimum 1.8 V. The more pressing issue with the behavior of these parts is the change in voltage during transient shutdowns, which is 2 V on V_{out}. The duration of these events is relatively short, meaning high frequency components are injected into the load which could be potentially damaging. These effects may be mitigated by integrating low-pass filters on the output of the device or input of sensitive ICs. Diode clipper circuits may also be utilized to ensure voltages do not exceed a given threshold [15], however, diodes too are susceptible to radiation effects, and a trade study must be performed to determine the optimal mitigation strategy for a system. Another approach to mitigation is derating, or reducing the electrical, mechanical, and or thermal stresses on a device such that the SEE response is dampened [53].

The 8A and 12A devices exhibited similar behavior during SEE testing. Both SET and SEFI were observed on the 12A device. All events have the same cross-section curve, thus one Weibull fit was performed for all events. Like the 8A device, the maximum recorded time for a POK event was 595 ms for a SEFI event. Typical POK events lasted a few milliseconds and V_{out} events for a few microseconds. Rapid changes

(a)   (b)

(c)   (d)
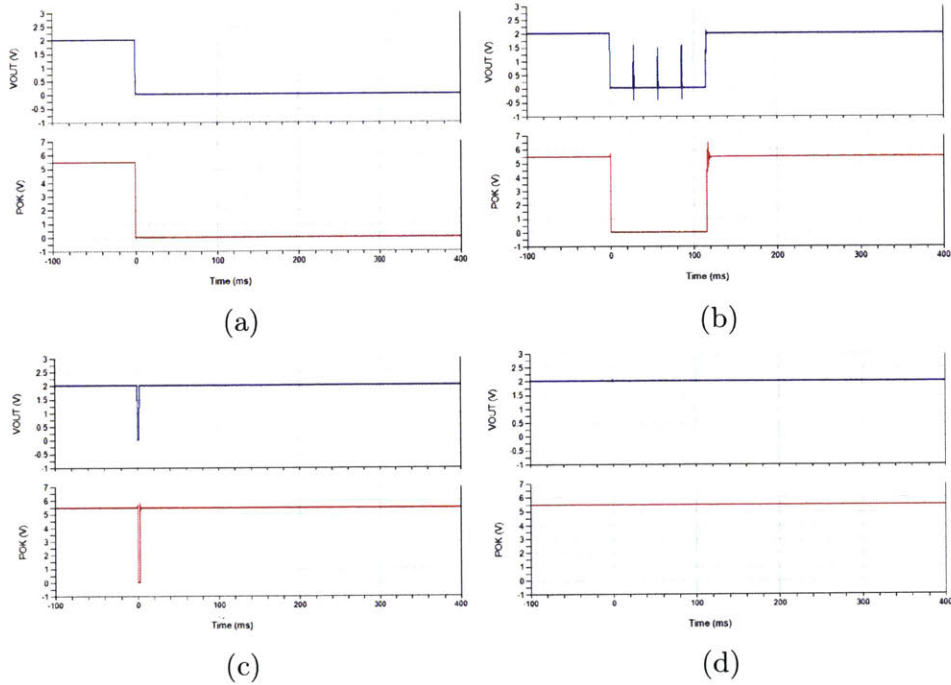
Figure 4-13: SEE events observed in th 8A device. a is persistent shutdown where POK and V_{out} fall to 0 V and require an external power cycle to return to nominal operations. b is a shutdown with attempt at restart that requires an external power cycle. c is a transient shutdown where the device autonomously returned to nominal operation. d is a V_{out} transient with little change to overall output level.

in output voltages, like the 8A device, are a concern when using this component. The same mitigation strategies for the 8A device can be used for the 12A since their response is similar.

4.2.1   Upset Rates

The cross-section curve illustrates the susceptibility of a device to SEE, but it is important to understand the implication of these values. Low LET threshold alone does not disqualify a device for space applications. Further analysis is required to determine the rate at which the device experiences SEE (*i.e.*, the upset rate). Knowing how often a device experiences SEE and the nature of the response is the basis for good mitigation strategies.

Upset rate calculations are done in OMERE 5.2.2 using the Weibull parameters for each cross-section curve. The radiation environment derived from orbital parameters

74
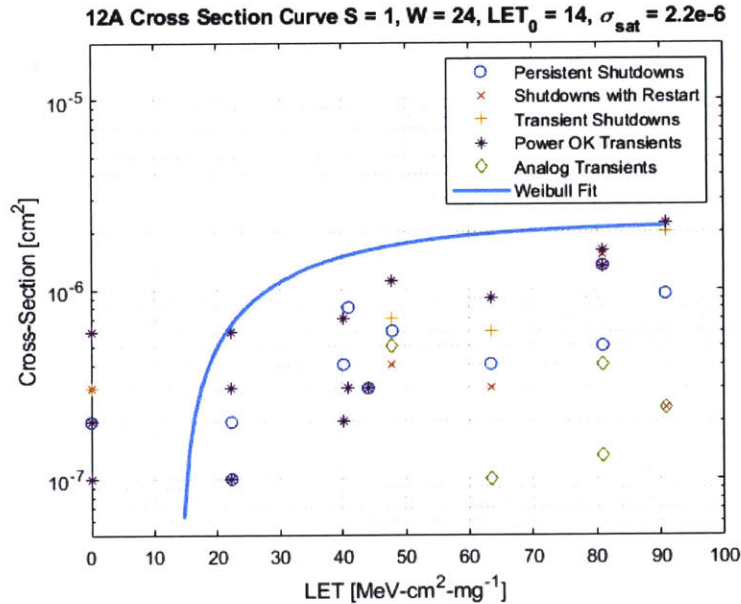
Figure 4-14: 12A Cross Section with S = 1 and W = 24. The onset LET is 14 MeV-cm^2-mg^{-1} and saturates at 2.2E-6 cm^2.

and lifetime is know. and used to calculate upset rates. Four environmental scenarios are used to calculate upset rates: GCR, solar flare worst 7-days, solar flare worst day, and solar flare worst 5 minutes. Note that upset rates were also analyzed for protons-only environments, however the LET threshold is high enough to exclude protons, and subsequent results showed no upsets induced by protons.

Cross-section curves can be highly sensitive to incidence direction. While the LET was increased from analysis to account for the cosine law, it is more difficult to induce SEE at normal incidence than angled, and the response of the device, in type and magnitude, can vary widely at angled incidence. Upset rates depend on cross-section, and lack of characterization away from normal incidence introduces uncertainty. As compensation, uncertainty is bounded through worst-case and best-estimate analyses. Tables 4.1 4.6 gives the best estimate and worst case upset rates for the 4A, 8A, and 12A devices for both missions with 200 mils of shielding.

Its apparent Telesat Polar evokes higher upset rates. This is attributed to higher energy particles incident on the spacecraft when orbiting outside the protection of the magnetic field.

75
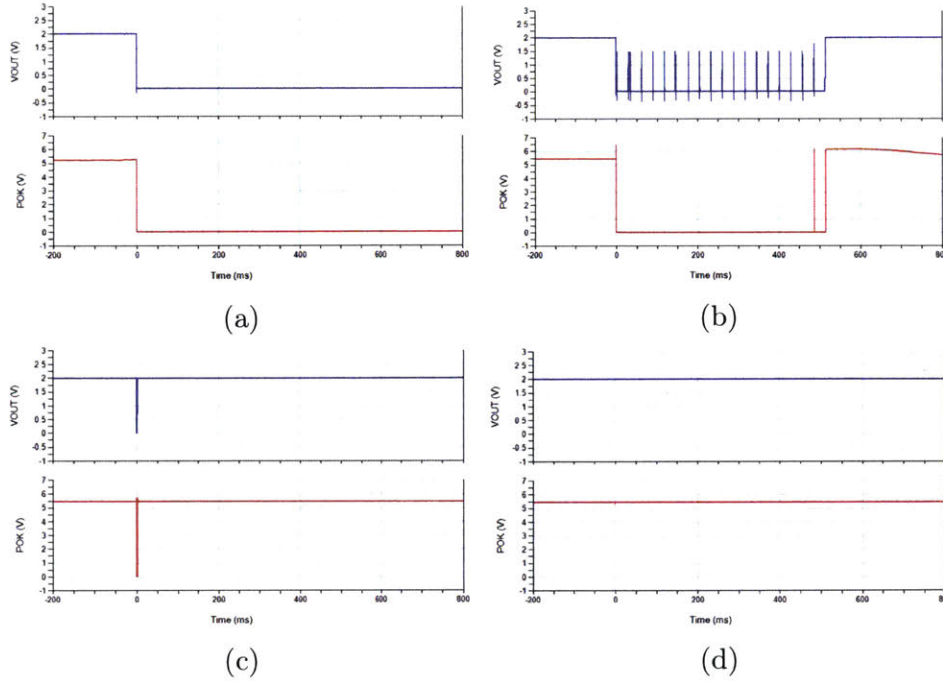
Figure 4-15: SEE Events in 12A Device. a is a persistent shutdown that requires external power cycling. b is a shutdown with restart event that requires external power cycling. c is a transient shutdown event. d is a V_{out} transient. Note that the oscilloscope was triggered to record an event, but the sampling rate was insufficient to capture the microsecond duration. Had an event been observed, it would have looked similar to c but with smaller amplitude change in POK.

Table 4.1: 4A Telesat Inclined Upset Rates

	Best Estimate (10.95 um) [events/device day]	Worst Case (0.55 um) [events/device day]
GCR	1.32e-9	1.21e-6
Flare (worst week)	1.65e-9	1.36e-6
Flare (worst day)	1.41e-9	1.24e-6
Flare (worst 5 min)	1.66e-9	1.31e-6

Table 4.2: 4A Telesat Polar Upset Rates

	Best Estimate (10.95 um) [events/device day]	Worst Case (0.55 um) [events/device day]
GCR	2.45e-6	7.32e-6
Flare (worst week)	1.18e-4	7.77e-4
Flare (worst day)	2.87e-4	3.28e-3
Flare (worst 5 min)	1.03e-3	1.21e-2

76

Table 4.3: 8A Telesat Inclined Upset Rates

	Best Estimate (2 um) [events/device day]	Worst Case (0.1 um) [events/device day]
GCR	3.4e-11	3.74e-8
Flare (worst week)	4.51e-11	4.24e-8
Flare (worst day)	3.69e-11	3.82e-8
Flare (worst 5 min)	4.56e-11	4.07e-8

Table 4.4: 8A Telesat Polar Upset Rates

	Best Estimate (2 um) [events/device day]	Worst Case (0.1 um) [events/device day]
GCR	8.43e-8	2.52e-7
Flare (worst week)	4.06e-6	2.71e-5
Flare (worst day)	9.89e-6	1.15e-4
Flare (worst 5 min)	3.54e-5	4.23e-4

Table 4.5: 12A Telesat Inclined Upset Rates

	Best Estimate (2.97 um) [events/device day]	Worst Case (0.15 um) [events/device day]
GCR	6.33e-11	7.11e-8
Flare (worst week)	8.43e-11	8.05e-8
Flare (worst day)	6.98e-11	7.26e-8
Flare (worst 5 min)	8.53e-11	7.74e-8

Table 4.6: 12A Telesat Polar Upset Rates

	Best Estimate (2.97 um) [events/device day]	Worst Case (0.15 um) [events/device day]
GCR	1.58e-7	4.81e-7
Flare (worst week)	7.63e-6	5.02e-5
Flare (worst day)	1.86e-5	2.11e-4
Flare (worst 5 min)	6.64e-5	7.78e-4

4.2.2 Failure Analysis

Once upset rates have been determined, reliability analysis is conducted. Reliability analysis reveals the risk associated with using a component. Using the highest upset rate, the 4A device for worst-case, 5 min flare, as a baseline, Eq 2.11 is applied to determine worst case reliability. The units for upset rate are in events/device-day, and must be converted to match units of time. The calculated reliability of this part

is 99.996%, which is well within MIL-STD-883 acceptance requirements [29]. This case is not reflective of flight conditions, so a second calculation with the highest rate 4A worst-case is done (Telesat Polar GCR). The time scale in the second calculation is much higher, and the reliability is 96.844%. For context, this reliability value is capturing the probability that the device does not experience a failure mode. In the case of the 4A device, the failure mode is a transient, which can be mitigated using methods mentioned above.

Each mission and program will have an established risk threshold in which a component will be accepted or rejected. For current space applications, the worst-case reliability of these parts is acceptable. These calculations illustrate that despite having an LET threshold under the minimum onset LET and a fairly high upset rate, the worst-case, worst-performing device is still a viable candidate for space applications with little additive risk.

Chapter 5

Conclusion and Future Work

5.1   Conclusion

In this thesis, three COTS buck DC-DC converters are tested based on the LEO space radiation environment, and their radiation response is characterized. Using COTS parts enables faster, cheaper, higher performance spacecraft designs. Few commercial DC-DC converters exist in NASA compendiums or literature, and those that do experienced latch-up, such as the Crane Interpoint Hybrid DC-DC converter [48], or likely have updated process flows, meaning performance characterization is irrelevant.

This work introduces the LEO radiation environment, including main radiation sources, and describes the effects relevant to semiconductor devices. Two next-generation LEO communications constellations are identified, and their orbit parameters are input into the modeling software OMERE 5.2.2 to derive TID, DD, and flux spectrum levels. Ionizing dose depth curves vs. shielding thickness are generated using a Shieldose-2 model. Non-ionizing dose depth curves vs. shielding thickness are generated using a target material of Silicon, the equivalent damage flux levels for a mono-energetic proton of 10 MeV in Silicon is calculated. The LET flux spectrum is generated, and a threshold flux of 10^{-7} is used to determine the highest imparted ion energy for each orbit with a given shielding thickness. Using 200 mils of shielding as a baseline, derived levels are used to inform TID and SEE testing (Table 2.4).

During TID testing, two samples of each DC-DC converter are tested to 100 krad(Si) or until device failure. The devices were subject to three loading conditions in-between radiation steps to test functionality of the device vs. dose. Device efficiency is most sensitive to ligh load conditions across all devices. The 4A device showed loss of functionality during TID testing between 60 and 70 krad(Si). The 4A device showed loss of functionality during TID testing between 60 and 70 krad(Si). The 8A and 12A devices showed loss of functionality during TID testing between 90 and 100 krad(Si). The gain of the devices decreased as a function of dose, which could indicate TID effects are manifesting in the control electronics, though no data provided conclusive evidence.

During SEE testing, at least two samples of each DC-DC converter are irradiated with heavy ions to an LET of at least 63 MeV-cm^2-mg^{-1}. SEE testing screened for destructive (latch-up) and non-destructive (transient) events. No latch-up is seen across any of the devices for all LET. Transients are seen across all parts at an LET 14 MeV-cm^2-mg^{-1}, and SEFIs are seen in the 8A and 12A device at an LET 14 MeV-cm^2-mg^{-1}.

Transient mitigation includes using low-pass filters on device outputs, including a clipping circuit, and or de-rating devices. The optimal solution transient mitigation for a system varies by mission and objectives, and a full trade study is required to select a mitigation strategy. The upset rates for each part are calculated using the OMERE models and device cross-sections. Reliability analysis is performed on the worst-case highest upset rate (4A in Telesat Polar) for two scenarios: GCR and Flare 5 min. Despite having a low LET threshold and high upset rate, reliability analysis reveals these devices are viable for space applications willing to accept slightly increased risk.

5.2   Future Work

The applied dose rate during TID testing is categorized as high by MIL-STD-883, which could lead to dose-dependent behavior. These devices should be tested at lower

dose rates to screen for this sensitivity. If no failure modes are observed and the dose rate is higher than the orbit dose rate, these parts can be considered TID tolerant to the maximum cumulative dose.

SEE testing revealed devices experiencing SEFI required external reset. The 12A and 8A devices have an enable pin that could provide a soft-restart, which is desirable alternative to power cycling the system. The enable pin toggle is not tested during SEE testing, but should be revisited for SEFI correction. Additionally, there is significant uncertainty in the Bragg peak, and particles with an estimated LET of 0 showed SEE in the devices. To reduce uncertainty in materials, the devices should be de-lidded and then re-irradiated.

In the context of space-based laser communication systems, this analysis would theoretically be one of many performed by the RHA team or engineer. The probability of success for electronics in the radiation environment across all subsystems hinges on early environment definition and clearly communicated radiation requirements. The RHA process is not confined to the component level, but rather extends from hardware and spacecraft layout to operations. While these DC-DC converters are low-risk, the RHA team must determine the total risk associated with using COTS parts throughout the spacecraft design.

Appendix A

Weibull Curve Estimation Code

```
% ——————————————————————
% Alexa  Aguilar
% Spring  2019
% DC DC SEE  Data  Processing
% Note:  Z(Au) = 79,  Z(Ta) = 73
% ——————————————————————

%%% 4A
 f_file  =  csvread ( '4_seedata.csv',1,0);
 f_fluence  =  f_file (:,4);      % fluence
 f_let  =  f_file (:,3);          % LET
 f_ps  =  f_file (:,5);           % persistent  shutdowns
 f_shr  =  f_file (:,6);          % shutdowns  with  restart
 f_trans  =  f_file (:,7);        % transient  shutdowns
 f_pok  =  f_file (:,8);          % power  ok  transients
 f_a_trans  =  f_file (:,9);      % analog  transients
 f_t_pok  =  f_file (:,10);       % max  pok  low

% Calculate  cross  section  for  each  event
 fsig_ps  =  f_ps./ f_fluence;
 fsig_shr  =  f_shr./ f_fluence;
 fsig_trans  =  f_trans./ f_fluence;
 fsig_pok  =  f_pok./ f_fluence;
 fsig_a_trans  =  f_a_trans./ f_fluence;

 f_let_0  =  14;    % from  observation

% Weibull  fit
 fsig_sat  =  round(max([max(fsig_a_trans),max(fsig_pok),
```

```matlab
  ...max( fsig_ps ) ,max( fsig_shr ) ,max( fsig_trans )]) *1.5 ,5 );
f_W = 20;
f_S = 1;
flin_let = linspace (min( f_let ) ,max( f_let ));
f_sig = fsig_sat *(1-exp (((  f_let_0 -  flin_let )./f_W ).^ f_S ));

% Plot
figure
semilogy ( f_let , fsig_ps , 'o' )
hold on
semilogy ( f_let , fsig_shr , 'x' )
semilogy ( f_let , fsig_trans , '+' )
semilogy ( f_let , fsig_pok , '*' )
semilogy ( f_let , fsig_a_trans , 'd' )
grid on
semilogy ( flin_let , f_sig , 'LineWidth' ,2)
axis ([0  100  1e-7  1e -3])
legend ( 'Persistent  Shutdowns' , 'Shutdowns  with
    Restart' , 'Transient  Shutdowns'
... , 'Power  OK  Transients' , 'Analog  Transients' , 'Weibull  Fit' )
ylabel ( 'Cross-Section  [cm^2] ' )
xlabel ( 'LET  [MeV-cm^2-mg^{ -1}] ' )
title ( '4A  Cross  Section  Curve  S = 1,  W = 20,  LET_{0}  = 14,
    \sigma_{sat} = 3e-5' )

%% 8A
e_file = csvread ( '8_seedata.csv' ,1 ,0 );
e_fluence = e_file (: ,4 );      % fluence
e_let = e_file (: ,3 );          % LET
e_ps = e_file (: ,5 );           % persistent  shutdowns
e_shr = e_file (: ,6 );          % shutdowns  with  restart
e_trans = e_file (: ,7 );        % transient  shutdowns
e_pok = e_file (: ,8 );          % power  ok  transients
e_a_trans = e_file (: ,9 );      % analog  transients
e_t_pok = e_file (: ,10 );       % max  pok  low

% Calculate  cross  section  for  each  event
esig_ps = e_ps ./ e_fluence ;
esig_shr = e_shr ./ e_fluence ;
esig_trans = e_trans ./ e_fluence ;
esig_pok = e_pok ./ e_fluence ;
esig_a_trans = e_a_trans ./ e_fluence ;

e_let_0 = 14;    % from  observation
```

```matlab
% Weibull fit
esig_sat = ...
    round(max([max(esig_a_trans),max(esig_pok),max(esig_ps),...
    ...max(esig_shr),max(esig_trans)]),6);
e_W = 19;
e_S = 1;
elin_let = linspace(min(e_let),max(e_let));
e_sig = esig_sat*(1-exp(((e_let_0 - elin_let)./e_W).^e_S));

% Plot
figure
semilogy(e_let,esig_ps,'o')
hold on
semilogy(e_let,esig_shr,'x')
semilogy(e_let,esig_trans,'+')
semilogy(e_let,esig_pok,'*')
semilogy(e_let,esig_a_trans,'d')
grid on
semilogy(elin_let,e_sig,'LineWidth',2)
axis([0 100 3e-8 8e-6])
legend('Persistent Shutdowns','Shutdowns with Restart',...
    ...'Transient Shutdowns','Power OK Transients','Analog
    Transients','Weibull Fit')
ylabel('Cross-Section [cm^2]')
xlabel('LET [MeV-cm^2-mg^{-1}]')
title('8A Cross Section Curve S = 1, W = 19, LET_{0} = 14,
    \sigma_{sat} = 1e-6')

%% 12A
t_file = csvread('12_seedata.csv',1,0);
t_fluence = t_file(:,4);      % fluence
t_let = t_file(:,3);          % LET
t_ps = t_file(:,5);           % persistent shutdowns
t_shr = t_file(:,6);          % shutdowns with restart
t_trans = t_file(:,7);        % transient shutdowns
t_pok = t_file(:,8);          % power ok transients
t_a_trans = t_file(:,9);      % analog transients
t_t_pok = t_file(:,10);       % max pok low

% Calculate cross section for each event
tsig_ps = t_ps./t_fluence;
tsig_shr = t_shr./t_fluence;
tsig_trans = t_trans./t_fluence;
tsig_pok = t_pok./t_fluence;
tsig_a_trans = t_a_trans./t_fluence;
```

85

```
t_let_0 = 14;    % from observation

% Weibull fit
tsig_sat = max([max(tsig_a_trans),max(tsig_pok),
...max(tsig_ps),max(tsig_shr),max(tsig_trans)])*1;
t_W = 24;
t_S = 1;
tlin_let = linspace(min(t_let),max(t_let));
t_sig = tsig_sat*(1-exp(((t_let_0 - tlin_let)./t_W).^t_S));

% Plot
figure
semilogy(t_let,tsig_ps,'o')
hold on
semilogy(t_let,tsig_shr,'x')
semilogy(t_let,tsig_trans,'+')
semilogy(t_let,tsig_pok,'*')
semilogy(t_let,tsig_a_trans,'d')
grid on
semilogy(tlin_let,t_sig,'LineWidth',2)
axis([0 100 5e-8 2e-5])
legend('Persistent Shutdowns','Shutdowns with Restart',
...'Transient Shutdowns','Power OK Transients','Analog
    Transients','Weibull Fit')
ylabel('Cross-Section [cm^2]')
xlabel('LET [MeV-cm^2-mg^{-1}]')
title('12A Cross Section Curve S = 1, W = 24, LET_{0} = 14,
    \sigma_{sat} = 2.2e-6')
```

Bibliography

[1] Gregory R. Allen et al. "2017 Compendium of Recent Test Results of Single Event Effects Conducted by the Jet Propulsion Laboratory's Radiation Effects Group". In: *2017 IEEE Radiation Effects Data Workshop (REDW)*. IEEE, 2017, pp. 1–9. ISBN: 978-1-5090-4647-8. DOI: 10.1109/NSREC.2017.8115429. URL: http://ieeexplore.ieee.org/document/8115429/.

[2] American Institute of Aeronautics and Astronautics. *AIAA G-083-1999 Guide To Modeling Earth's Trapped Radiation Environment*. Tech. rep. 1999. URL: https://www.spacewx.com/Docs/AIAA{_}G-083-1999.pdf.

[3] Kenichi Araki et al. "Experimental operations of laser communication equipment onboard ETS-VI satellite". In: ed. by G. Stephen Mecherle. Vol. 2990. International Society for Optics and Photonics, 1997, pp. 264–275. DOI: 10.1117/12.273702. URL: http://proceedings.spiedigitallibrary.org/proceeding.aspx?articleid=1028219.

[4] ARM. *ARM1136J(F)-S*. 2009. URL: https://web.archive.org/web/20090321200633/http://www.arm.com/products/CPUs/ARM1136JF-S.html.

[5] BAE Systems. *BAE Systems' Current Processors and Single Board Computers*. Tech. rep. 2013. URL: https://www.baesystems.com/en/download-en/20190124214317/1434554723043.pdf.

[6] Robert Baumann. *Making the grade: From COTS to full space-grade*. 2018. URL: https://radiositysolutions.com/making-the-grade-from-cots-to-full-space-grade/ (visited on 05/13/2019).

87

[7]   Robert Baumann. *What's so great about single controlled baseline lots?* 2018. URL: https://radiositysolutions.com/whats-so-great-about-single-controlled-baseline-lots/ (visited on 05/13/2019).

[8]   Mark P Baze. "Single Event Effects in Digital and Linear ICs". In: *Proc. NSREC Tutorial Short Course.* 2011, pp. 1–61.

[9]   Melanie Berg et al. *Characterization of System Level Single Event Upset (SEU) Responses using SEU Data, Classical Reliability Models, and Space Environment Data.* 2017. URL: https://ntrs.nasa.gov/search.jsp?R=20170005807.

[10]   Don M. Boroson and Bryan S. Robinson. "The lunar laser communication demonstration nasafirst step toward very high data rate support of science and exploration missions". In: *The Lunar Atmosphere and Dust Environment Explorer Mission (LADEE).* Springer International Publishing, 2015, pp. 115–128. ISBN: 9783319187174. DOI: 10.1007/978-3-319-18717-4_6.

[11]   Don M. Boroson et al. "Overview and results of the Lunar Laser Communication Demonstration". In: ed. by Hamid Hemmati and Don M. Boroson. Vol. 8971. International Society for Optics and Photonics, 2014, 89710S. DOI: 10.1117/12.2045508. URL: http://proceedings.spiedigitallibrary.org/proceeding.aspx?doi=10.1117/12.2045508.

[12]   Brookhaven National Laboratory (Organization). *NSRL User Guide — Technical Data Beam Ion Species and Energies.* URL: https://www.bnl.gov/nsrl/userguide/beam-ion-species-and-energies.php (visited on 05/13/2019).

[13]   Ying Cheng and Zhongming Ye. *Tiny, High Efficiency Monolithic Regulators Power Advanced SoCs and Microprocessors Feature Silent Switcher 2 Technology for Low EMI.* Tech. rep. URL: https://www.analog.com/media/en/technical-documentation/tech-articles/Tiny-High-Efficiency-Monolithic-Regulators-Power-Advanced-SoCs-and-uProcessors-Feature-Silent-Switcher-2-Technology-for-Low-EMI.pdf.

[14] P. E. Dodd et al. "Current and Future Challenges in Radiation Effects on CMOS Electronics". In: *IEEE Transactions on Nuclear Science* 57.4 (2010), pp. 1747–1763. ISSN: 0018-9499. DOI: 10.1109/TNS.2010.2042613. URL: http://ieeexplore.ieee.org/document/5550487/.

[15] Electronics Tutorials (Website). *Diode Clipping Circuits and Diode Clipper.* URL: https://www.electronics-tutorials.ws/diode/diode-clipping-circuits.html (visited on 05/13/2019).

[16] European Space Agency; European Coorporation for Space Standarization. *Space engineering Space environment ECSS Secretariat ESA-ESTEC Requirements; Standards Division Noordwijk, The Netherlands.* Tech. rep. 2008. URL: https://www.spacewx.com/Docs/ECSS-E-ST-10-04C{_}15Nov2008.pdf.

[17] "Far-field pattern measurement of an onboard laser transmitter by use of a space-to-ground optical link". In: *Applied Optics* 37.10 (1998), p. 1720. ISSN: 0003-6935. DOI: 10.1364/AO.37.001720. URL: https://www.osapublishing.org/abstract.cfm?URI=ao-37-10-1720.

[18] FCC (Organization). *Application for Fixed Satellite Service by Telesat Canada [SAT-PDR-20161115-00108].* URL: https://fcc.report/IBFS/SAT-PDR-20161115-00108 (visited on 05/13/2019).

[19] *Federal Communications Commission NOTICE OF PROPOSED RULEMAKING *.* URL: https://apps.fcc.gov/edocs{_}public/attachmatch/DOC-346552A1.pdf (visited on 05/10/2019).

[20] Renny Fields et al. "NFIRE-to-TerraSAR-X laser communication results: satellite pointing, disturbances, and other attributes consistent with successful performance". In: ed. by Joseph L. Cox and Pejmun Motaghedi. Vol. 7330. International Society for Optics and Photonics, 2009, 73300Q. DOI: 10.1117/12.820393. URL: http://proceedings.spiedigitallibrary.org/proceeding.aspx?doi=10.1117/12.820393.

[21] G.D. Fletcher, T.R. Hicks, and B. Laurent. "The SILEX optical interorbit link experiment". In: *Electronics & Communications Engineering Journal* 3.6 (1991), p. 273. ISSN: 09540695. DOI: 10.1049/ecej:19910045. URL: https://digital-library.theiet.org/content/journals/10.1049/ecej{_}19910045.

[22] Henry B Garrett and Insoo Jun. "Spacecraft Environment Interactions". In: *Proc. NSREC Tutorial Short Course*. 2011.

[23] Brigitte Hauke. *Basic Calculation of a Buck Converter's Power Stage*. Tech. rep. 2011. URL: www.ti.com.

[24] Hamid Hemmati, ed. *Near-Earth Laser Communications*. CRC Press, 2018. ISBN: 9781315221427. DOI: 10.1201/9781420015447. URL: https://www.taylorfrancis.com/books/9781420015447.

[25] Caleb Henry. *FCC issues warning in wake of Swarm's unauthorized launch*. 2018. URL: https://spacenews.com/fcc-issues-warning-in-wake-of-swarms-unauthorized-launch/ (visited on 05/10/2019).

[26] "High-Performance Embedded Computing in Space: Evaluation of Platforms for Vision-Based Navigation". In: *Journal of Aerospace Information Systems* 15.4 (2018), pp. 178–192. ISSN: 2327-3097. DOI: 10.2514/1.I010555. URL: https://arc.aiaa.org/doi/10.2514/1.I010555.

[27] HiRel AG Infineon Technology. *HYBRID-HIGH RELIABILITY RADIATION HARDENED DC-DC CONVERTER LSO LSO SERIES Description*. Tech. rep. URL: http://www.irf.com/product-info/datasheets/data/lso28.pdf.

[28] International Technology Roadmap for Semiconductors. *International Technology Roadmap for Semiconductors 2015 Edition More Moore*. Tech. rep. 2015. URL: https://www.semiconductors.org/wp-content/uploads/2018/06/5{_}2015-ITRS-2.0{_}More-Moore.pdf.

[29] JEDEC Solid State Technology Association. *JEDEC STANDARD Requirements for Microelectronic Screening and Test Optimization JEP121A*. Tech. rep. 2006. URL: `https://www.jedec.org/taxonomy/term/2754`.

[30] JEDEC SOLID STATE TECHNOLOGY ASSOCIATION (Organization). *JEDEC STANDARD Test Procedures for the Measurement of Single-Event Effects in Semiconductor Devices from Heavy Ion Irradiation JESD57A*. Tech. rep. 2017. URL: `www.jedec.org`.

[31] Jet Propulsion Laboratory. *Mars Science Laboratory/Curiosity*. Tech. rep. URL: `https://www.jpl.nasa.gov/news/fact{\_}sheets/mars-science-laboratory.pdf`.

[32] Jet Propulsion Laboratory. *Method for Calculating Heavy-Ion Induced SEU Rates*. Tech. rep. Jet Propulsion Laboratory.

[33] Takashi Jono et al. "OICETS on-orbit laser communication experiments". In: *Free-Space Laser Communication Technologies XVIII* 6105.May (2006), p. 610503. DOI: `10.1117/12.673751`.

[34] John Keller. *The evolving world of radiation-hardened electronics*. 2018. URL: `https://www.militaryaerospace.com/articles/print/volume-29/issue-6/technology-focus/the-evolving-world-of-radiation-hardened-electronics.html` (visited on 05/10/2019).

[35] K.A. LaBel et al. "Emerging radiation hardness assurance (RHA) issues: a NASA approach for space flight programs". In: *IEEE Transactions on Nuclear Science* 45.6 (1998), pp. 2727–2736. ISSN: 00189499. DOI: `10.1109/23.736521`. URL: `http://ieeexplore.ieee.org/document/736521/`.

[36] Kenneth Label and Michael Sampson. *Thoughts on Commercial Off the Shelf (COTS) Electronics for Space or There's No Radiation Hardened Radio Shack on the Moon*. Tech. rep. 2013. URL: `https://nepp.nasa.gov/workshops/etw2013/talks/Tue_June11_2013/1030_LaBel_Sampson_Thoughts\%20on\%20COTS\%20Electronics\%20for\%20Space.pdf`.

[37] Kenneth A. LaBel and Steven M. Guertin. "NASA Past, Present, and Future: The Use of Commercial Off The Shelf (COTS) Electronics in Space". In: (2017). URL: https://ntrs.nasa.gov/search.jsp?R=20170003048.

[38] Ray Ladbury. *Strategies for SEE Hardness Assurance-Form Buy-It-And-Fly-It to Bullet Proof.* Tech. rep. URL: https://ntrs.nasa.gov/search.jsp?R=20170006865.

[39] Jean-Marie Lauenstein. *Test Standard Revision Update: JESD57, Procedures for the Measurement of Single-Event Effects in Semiconductor Devices from Heavy-Ion Irradiation.* Tech. rep. 2015. URL: https://nepp.nasa.gov/workshops/etw2015/talks/25-Thu/0900-2015-561-Lauenstein-Final-Pres-NEPP-ETW-JESD57-TN24561.pdf.

[40] Thuy Mai. *Benefits of Optical Communications.* 2013. URL: https://www.nasa.gov/content/benefits-of-optical-communications/ (visited on 05/10/2019).

[41] MIT Lincoln Laboratory. *Don M. Boroson Biography.* URL: https://www.ll.mit.edu/biographies/don-m-boroson (visited on 05/12/2019).

[42] MIT Lincoln Laboratory. *Roy S. Bondurant Biography.* URL: https://www.ll.mit.edu/biographies/roy-s-bondurant (visited on 05/12/2019).

[43] Morgan Stanley (Organization). *Get Ready for the Data Decade.* 2018. URL: https://www.morganstanley.com/ideas/data-decade (visited on 05/10/2019).

[44] Naitonal Institute of Standards and Technology. *Bathtub Curve.* URL: https://www.itl.nist.gov/div898/handbook/apr/section1/apr124.htm (visited on 05/10/2019).

[45] National Telecommunications and Information Administration. *United States Frequency Allocation Chart.* URL: https://www.ntia.doc.gov/page/2011/united-states-frequency-allocation-chart (visited on 05/13/2019).

[46] R. A. Nymmik, M. I. Panasyuk, and A. A. Suslov. "Galactic cosmic ray flux simulation and prediction". In: *Advances in Space Research* 17.2 (1996), pp. 19–30. DOI: `10.1016/0273-1177(95)00508-C`. URL: `https://www-sciencedirect-com.libproxy.mit.edu/science/article/pii/027311779500508C`.

[47] Bogdan V. Oaida et al. "Optical link design and validation testing of the Optical Payload for Lasercomm Science (OPALS) system". In: ed. by Hamid Hemmati and Don M. Boroson. Vol. 8971. International Society for Optics and Photonics, 2014, 89710U. DOI: `10.1117/12.2045351`. URL: `http://proceedings.spiedigitallibrary.org/proceeding.aspx?doi=10.1117/12.2045351`.

[48] Martha V. O'Bryan et al. "Compendium of Current Single Event Effects Results from NASA Goddard Space Flight Center and NASA Electronic Parts and Packaging Program". In: *IEEE Nuclear and Space Radiation Effects Conference* (2017). URL: `https://ntrs.nasa.gov/search.jsp?R=20170008448`.

[49] Timothy R Oldham. "Basic mechanisms of TID and DDD response in MOS and bipolar microelectronics". In: *Proc. NSREC Tutorial Short Course*. 2011, pp. 1–95.

[50] OneWeb. *About Us OneWeb Satellites*. URL: `https://onewebsatellites.com/about-us/` (visited on 05/20/2019).

[51] Jeannette Plante. *Cost Impacts of Upgrading Electronic Parts for Use in NASA Space Flight Systems*. Tech. rep. 2002. URL: `http://nepp.nasa.gov/npsl/`.

[52] Power Electronics (Website). *Rad-Hard Low-Voltage DC-DC Converters Serve Satellite Power Systems*. 2013. URL: `https://www.powerelectronics.com/dc-dc-converters/rad-hard-low-voltage-dc-dc-converters-serve-satellite-power-systems` (visited on 05/13/2019).

[53] *PREFERRED RELIABILITY PRACTICES PRACTICE NO. PD-ED-1201 PAGE 1 OF 3 EEE PARTS DERATING*. Tech. rep. URL: `http://www.klabs.org/DEI/References/design{\_}guidelines/design{\_}series/1201.pdf`.

[54] Dianne Ramirez. *Laser Communications Demonstrated from CubeSats for the First Time*. 2018. URL: `https://aerospace.org/press-release/laser-communications-demonstrated-cubesats-first-time` (visited on 05/12/2019).

[55] T S Rose et al. *Optical Communications Downlink from a 1.5U CubeSat: OCSD Program*. Tech. rep. 2018. URL: `https://digitalcommons.usu.edu/cgi/viewcontent.cgi?article=4298{\&}context=smallsat`.

[56] Andreas Schutz. *DLR communicates with TerraSAR-X Earth Observation satellite via laser beam*. URL: `https://www.dlr.de/en/desktopdefault.aspx/tabid-78/7420{\_}read-14120/` (visited on 05/12/2019).

[57] S. Seltzer. *SHIELDOSE: a computer code for Space-Shielding Radiation Dose Calculations. Final report*. Tech. rep. National Bureau of Standards, 1980. URL: `https://inis.iaea.org/search/search.aspx?orig{\_}q=RN:12598344`.

[58] Spaceflight. *New Federal Policy Would Hike Student Spacecraft Costs, Threatening Tech Education*. 2018. URL: `https://www.space.com/40761-federal-policy-hikes-student-spacecraft-costs.html`.

[59] *STK - Object Tools - Walker*. URL: `http://help.agi.com/stk/index.htm{\#}stk/tools-12.htm` (visited on 05/21/2019).

[60] Texas Instruments. *TPS54334 4.2-V to 28-V Input Voltage, 3-A Output Current Synchronous Step-Down Voltage Converter*. Tech. rep. 2015. URL: `www.ti.com`.

[61] A.J. Tylka et al. "CREME96: A Revision of the Cosmic Ray Effects on Micro-Electronics Code". In: *IEEE Transactions on Nuclear Science* 44.6 (1997), pp. 2150–2160. DOI: `10.1109/23.659030`. URL: `http://ieeexplore.ieee.org/document/659030/`.

[62] M.A. Xapsos et al. "Model for solar proton risk assessment". In: *IEEE Transactions on Nuclear Science* 51.6 (2004), pp. 3394–3398. ISSN: 0018-9499. DOI: `10.1109/TNS.2004.839159`. URL: `http://ieeexplore.ieee.org/document/1369501/`.

[63] M.A. Xapsos et al. "Probability model for cumulative solar proton event fluences". In: *IEEE Transactions on Nuclear Science* 47.3 (2000), pp. 486–490. ISSN: 0018-9499. DOI: 10.1109/23.856469. URL: http://ieeexplore.ieee.org/document/856469/.

[64] H. Zech et al. "LCT for EDRS: LEO to GEO optical communications at 1,8 Gbps between Alphasat and Sentinel 1a". In: ed. by Edward M. Carapezza et al. Vol. 9647. International Society for Optics and Photonics, 2015, 96470J. DOI: 10.1117/12.2196273. URL: http://proceedings.spiedigitallibrary.org/proceeding.aspx?doi=10.1117/12.2196273.